Monthly Notices of the ROYAL ASTRONOMICAL SOCIETY

MNRAS **527,** 6473–6494 (2024)
Advance Access publication 2023 November 27

https://doi.org/10.1093/mnras/stad3655

Detailed spectrophotometric analysis of the superluminous and fast evolving SN 2019neq

Achille Fiore [1,2★] Stefano Benetti [2★] Leonardo Tartaglia,[2,3] Anders Jerkstrand,[4] Irene Salmaso,[2,5] Lina Tomasella [2] Antonia Morales-Garoffolo,[6] Stefan Geier,[7,8] Nancy Elias-Rosa,[2,9] Enrico Cappellaro,[2] Xiaofeng Wang,[10,11] Jun Mo,[10] Zhihao Chen,[10] Shengyu Yan,[10] Andrea Pastorello,[2] Paolo A. Mazzali,[12,13] Riccardo Ciolfi [2,14] Yongzhi Cai [15,16,17] Morgan Fraser [18] Claudia P. Gutiérrez [19,20] Emir Karamehmetoglu,[4,21] Hanindyo Kuncarayakti,[22] Shane Moran,[22] Paolo Ochner,[2,5] Andrea Reguitti [2,23] Thomas M. Reynolds [22,24] and Giorgio Valerin[2,5]

Affiliations are listed at the end of the paper

Accepted 2023 November 21. Received 2023 November 17; in original form 2023 April 26

ABSTRACT

SN 2019neq was a very fast evolving superluminous supernova. At a redshift $z = 0.1059$, its peak absolute magnitude was -21.5 ± 0.2 mag in g band. In this work, we present data and analysis from an extensive spectrophotometric follow-up campaign using multiple observational facilities. Thanks to a nebular spectrum of SN 2019neq, we investigated some of the properties of the host galaxy at the location of SN 2019neq and found that its metallicity and specific star formation rate are in a good agreement with those usually measured for SLSNe-I hosts. We then discuss the plausibility of the magnetar and the circumstellar interaction scenarios to explain the observed light curves, and interpret a nebular spectrum of SN 2019neq using published SUMO radiative-transfer models. The results of our analysis suggest that the spin-down radiation of a millisecond magnetar with a magnetic field $B \simeq 6 \times 10^{14}$ G could boost the luminosity of SN 2019neq.

Key words: supernovae: general – supernovae: individual: SN 2019neq.

1 INTRODUCTION

It is widely accepted that supernovae (SNe) are a possible final stage of the life of massive stars and white dwarfs in close binary systems; they are observationally classified as type-I (SNe I) or type-II (SNe II) depending on whether they are hydrogen-poor or hydrogen-rich, respectively. SNe are usually discovered by untargeted wide-field surveys and they can be identified in their local environment performing differential photometry (see also section 2 and Kessler et al. 2015): in fact, their light curves (LCs) have a magnitude at maximum spanning the range -14 to -19 mag in the optical bands. SN light curves are normally interpreted as being powered by ^{56}Ni radioactive decay (e. g. Nadyozhin 1994) and by the energy deposited in the ejecta by the shock break-out. However, observations of the so-called superluminous SNe (SLSNe) have complicated this picture, as their absolute magnitude at maximum can be even brighter than -21 mag in optical bands (e.g. Gal-Yam 2012, 2019). Similar to their lower luminosity siblings, these events are grouped in SLSNe I and SLSNe II based on the strength of their H features, however their luminosity cannot be comfortably explained by the energy released from ^{56}Ni decay if the classical neutrino-wind driven core–collapse scenario is assumed. In fact, the explosion of standard SN progenitors synthesizes $\sim 0.1\,M_\odot$, while SLSNe require $\gtrsim 1 - 10\,M_\odot$ of ^{56}Ni (e.g. Umeda & Nomoto 2008; Gal-Yam et al. 2009; Kasen, Woosley & Heger 2011; Dessart et al. 2012). In principle, the explosion of a pair-instability SN (e. g. Yoshida et al. 2016) is a channel to synthesize much more ^{56}Ni than standard core–collapse SNe, but this scenario is disfavoured by the observed spectra of SLSNe (see e.g. Kozyreva & Blinnikov 2015; Mazzali et al. 2019; Moriya, Mazzali & Tanaka 2019). Two main alternatives have been considered to reproduce the observational properties of SLSNe. The first requires a shock where the SN ejecta collides with circumstellar material (CSM) lost by the progenitor star before its explosion (Woosley, Blinnikov & Heger 2007; Sorokina et al. 2016; Tolstov et al. 2017; Woosley 2017). In this scenario, the shock driven by their SN ejecta converts the kinetic energy in radiation via collisional excitation and ionization processes. Alternatively, the deposition in the ejecta of the spin-down radiation of a newly born, highly magnetized neutron star (a magnetar; e.g. Woosley, Blinnikov & Heger 2007; Kasen & Bildsten 2010) can boost SLSNe luminosities. However, the magnetar model does not naturally predict the bumps often seen in SLSNe-I LCs both before and after maximum (see e.g. Nicholl et al. 2016a; Smith et al. 2016; Nicholl, Guillochon & Berger 2017; Vreeswijk et al. 2017; Lunnan et al. 2020; Fiore et al. 2021; Gutiérrez et al. 2022; Chen et al. 2023a, b; Lin et al. 2023; West et al. 2023; but see Moriya et al. 2022) but is able to account for the huge variety of LC evolutionary time-scales shown by SLSNe I

★ E-mail: achillefiore@gmail.com (AF); stefano.benetti@inaf.it (SB)

(Chatzopoulos et al. 2013; Inserra et al. 2013; Nicholl et al. 2014, 2015a; Nicholl, Guillochon & Berger 2017).

Observationally, SLSNe I have blue spectra (with a blackbody temperature spanning $T_{BB} = 10\,000$–$20\,000$ K) during the pre-maximum/maximum phases, with prominent absorptions between 3000 and 5000 Å. These features are usually identified as O II (e.g. Mazzali et al. 2016), although there is no general consensus on this (as discussed later). After 2–3 weeks from maximum, SLSNe I enter a new phase in which their spectra bear a resemblance to those of broad lined SNe Ic (SNe Ic BL) at their maximum luminosity (e.g. Pastorello et al. 2010). Photometrically, their LCs are very heterogeneous and may evolve over a wide range of time-scales (see e.g. fig. 5 of De Cia et al. 2018). Inserra et al. (2018) suggested to distinctly separate rapidly declining SLSNe I from slow ones, but larger SLSNe-I samples point towards a continuous distribution of time-scales (Nicholl et al. 2015a; De Cia et al. 2018; Lunnan et al. 2018; Angus et al. 2019). Recently, Könyves-Tóth & Vinkó (2021) and Könyves-Tóth (2022) proposed a new SLSNe-I subclassification based on their features in pre-maximum/maximum spectra: type-W SLSNe I, whose absorptions are well fitted by O II at reasonable velocities and type-15bn SLSNe I, whose early spectral features are not easily explained by O II and show similarities with the coeval spectra of SN 2015bn (Nicholl et al. 2016a).

In this work, we deal with the SLSN I SN 2019neq, which was classified by Könyves-Tóth & Vinkó (2021) in the type-W subgroup. At a redshift $z \simeq 0.1059$ (see Section 3), SN 2019neq is located at RA = $17^{h}54^{m}26\overset{s}{.}736$, Dec = $+47^{\circ}15'40\overset{''}{.}62$ and it is likely associated with the galaxy SDSS J175426.70+471542.3. It was discovered on 2019 August 9 by the Zwicky Transient Facility (ZTF; Bellm et al. 2019) with an apparent magnitude of $g = 20.4$ mag (Perley et al. 2019), and named with the internal designation of ZTF19abpbopt. A few days later, a spectrum observed with the Palomar 60-inch + SED Machine revealed a hot continuum with some unidentified features (Perley et al. 2019). After ∼18 d, a spectrum of SN 2019neq was taken at the Liverpool Telescope (LT; Steele et al. 2004) (Roque de Los Muchachos Observatory, La Palma, Spain) equipped with the SPRAT (SPectrograph for the Rapid Acquisition of Transients, Piascik et al. 2014) instrument and classified as a SLSN I (Könyves-Tóth et al. 2019). A $g = 17.2$ mag detection implied that it was still in the rising phase with a rest-frame rate of ~ 0.2 mag d^{-1}.

SN 2019neq was already included in several studies: Könyves-Tóth et al. (2020) presented and discussed the ZTF photometry of SN 2019neq and three photospheric spectra. Furthermore, SN 2019neq was included in four sample papers (Hosseinzadeh et al. 2022; Chen et al. 2023a, b; Pursiainen et al. 2023): in particular, Hosseinzadeh et al. (2022) and Chen et al. (2023a, b) interpret post-maximum undulations in the *g*- and *r*-filter LCs of SN 2019neq as SLSNe-I bumps, i.e. they attributed the undulations either to a variable energy source or to an external one (e.g. CSM interaction). Pursiainen et al. (2023) analysed linear-polarimetry data of 7 H-poor SLSNe I and concluded that SLSNe I with oscillating LCs usually show an increase of the degree of polarimetry: therein, SN 2019neq was included in the non-oscillating SLSNe I subsample. In this work, we present a deep photometric and spectroscopic data set of SN 2019neq and, based on new coeval photometry, disfavour that the undulations seen in its *g*- and *r*-filters LCs have an astrophysical origin. Our analysis is in agreement with the ejecta mass estimated by Könyves-Tóth et al. (2020) in an independent way.

In detail, in Sections 2 and 3 we introduce the photometric and the spectroscopic observations of SN 2019neq, respectively; in Section 4 we compare SN 2019neq LCs and spectra with other SLSNe I (Section 4.1), we study its colour and temperature evolution (Section 4.2), and the evolution of its expansion velocity via the O II spectral absorption features (Section 4.3). Finally, we discuss the magnetar and the CSM-interaction interpretations (Section 4.4) using the nebular spectrum of SN 2019neq (Section 4.4.1) and modelling its observed multicolour LCs (Section 4.4.2). Throughout the paper, we will assume a flat Universe with $\Omega_M = 0.31$, $\Omega_\Lambda = 0.69$, and with a Hubble constant $H_0 = 71 \pm 3$ km s^{-1} Mpc^{-1}; we took this value of H_0 as an average among the estimates provided by Planck Collaboration XIII (2016), Khetan et al. (2021), and Riess et al. (2021).

2 PHOTOMETRY

2.1 Observations and data reductions

Ultraviolet/optical/near-infrared imaging data of SN 2019neq were obtained via different facilities. In detail, we used the NOT Unbiased Transients Survey 2 (NUTS2;[1] Mattila et al. 2016; Holmbo et al. 2019) at the 2.56-m Nordic Optical Telescope (NOT)+ALFOSC/NOTCam, the 2.0-m Liverpool Telescope (LT)+IO:O, La Palma observatory, Spain; the 1.82-m Copernico Telescope+AFOSC and Schmidt telescopes at the Asiago Astrophysical Observatory, Italy; the Tsinghua-NAOC (National Astronomical Observatories of China) Telescope (TNT) + BFOSC (Beijing Faint Object Spectrograph and Camera), Xinglong Observatory, China (Wang et al. 2008; Huang et al. 2015). *uvw*2, *uvm*2, *uvw*1, *U*, *B*, *V* follow up was triggered with the *Neil Gehrels Swift* Observatory + Ultraviolet/Optical Telescope (UVOT; Gehrels et al. 2004). *Swift*/UVOT *uvw*2, *uvm*2, *uvw*1, *U*, *B*, *V*-filter frames were reduced[2] with the HEASOFT package [version 6.25 (HEASARC) 2014]. The ground-based *u*, *B*, *V*, *g*, *r*, *i*, *z* photometric frames were preliminary pre-processed, i.e. they were corrected for overscan, bias, and flat field. Magnitude measurements were performed by means of the ECSNOOPY pacakage[3] (Cappellaro 2014). Before measuring the SN flux, we accounted for the contribution of the background contaminating the SN light either with a polynomial interpolation or with the template-subtraction technique. The latter was performed with the HOTPANTS tool (Becker 2015). When possible, we used template frames obtained with the same instrumental setting used for the scientific observations and observed after that the SN faded well below the detection limit. When deep template frames were not available, we estimated the background contribution interpolating a low-order polynomial to the area surrounding the SN position. This was interpreted as the background level and then subtracted from the photometric frames contaminated by the SN background. SN magnitudes were then measured fitting a point spread function to the SN (Stetson 1987). A detailed description of the image reduction and measurements procedures can be found in Fiore et al. (2021). Instrumental *u*, *B*, *g*, *V*, *r*, *i*, *z* magnitudes were calibrated on a sequence of non-saturated field stars from the SDSS (Sloan Digital Sky Survey) and the Pan-STARRS (Panoramic Survey Telescope and Rapid Response System; Chambers et al. 2016) surveys, respectively. For *U*, *B*, *V* filters, we converted the reference star magnitudes from Sloan to Johnson system following Chonis & Gaskell (2008). *J*, *H*,

[1] https://nuts.sn.ie

[2] Their calibration was done using the updated version (2020 November) of the sensitivity corrections.

[3] ECSNOOPY is a python package for SN photometry using PSF fitting and/or template subtraction developed by E. Cappellaro. A package description can be found at http://sngroup.oapd.inaf.it/.

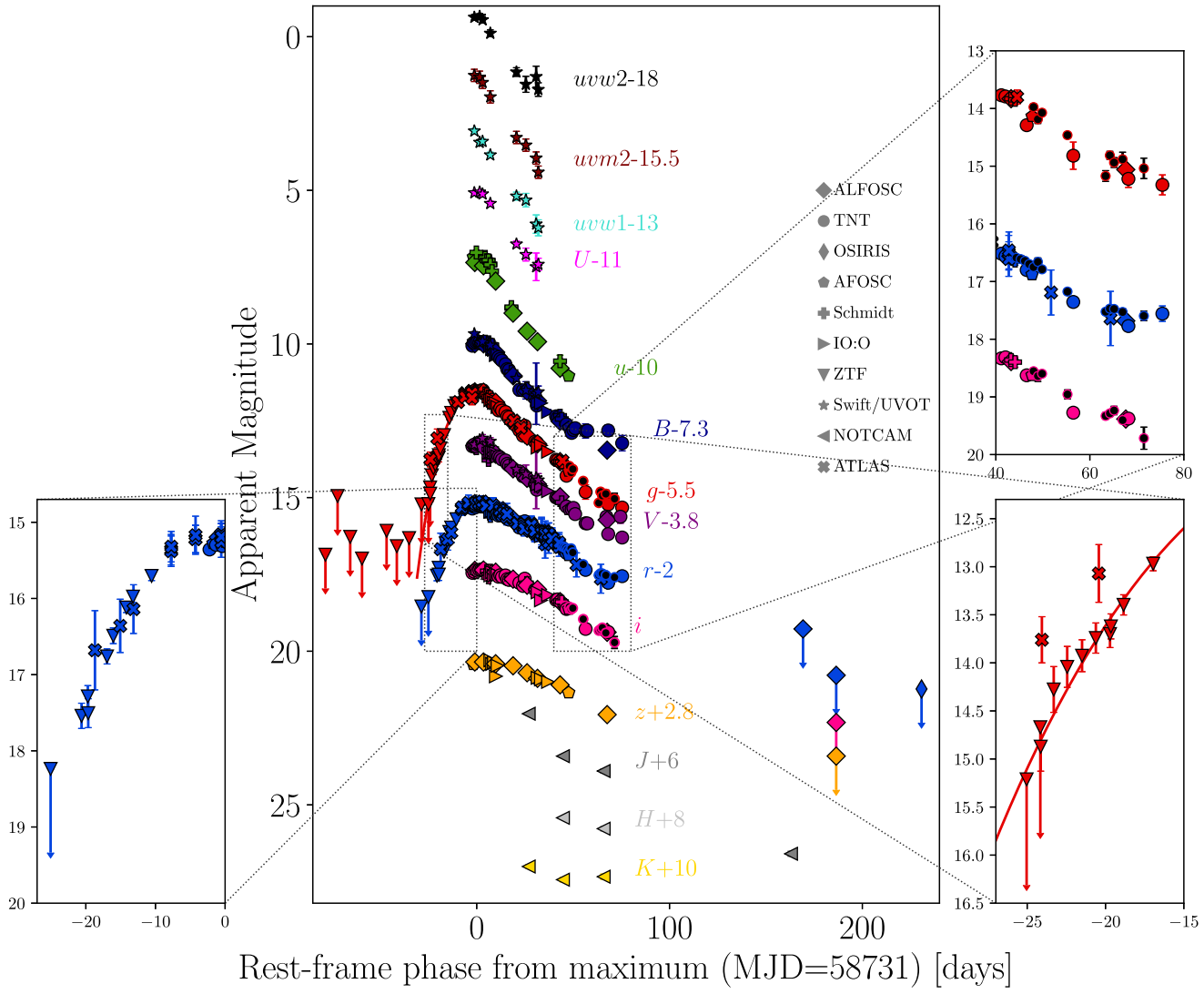

Figure 1. S-corrected light curves for SN 2019neq in *uvw*2, *uvm*2, *uvw*1, *U*, *u*, *B*, *g*, *V*, *r*, *i*, *z*, *J*, *H*, K_s bands (each LC is labelled on its right-hand side). Photometry obtained with different instruments are plotted with different symbols, as labelled in the upper right-hand corner. The *g*-filter LC was fitted with a high-order polynomial (red solid line) to obtain the epoch of maximum luminosity (see the text). Arrows correspond to 2.5σ detection limits. Magnitudes are in the AB system. The upper inset on the right-hand side shows the period in which the late bump is visible [additional data from Hosseinzadeh et al. (2022) are represented by black dots]; the lower-left and lower-right insets show the pre-maximum phases in *r* and *g* filters, respectively.

K_s magnitudes were calibrated with reference to field stars present in the 2MASS catalogue (Two-Micron All Sky Survey; Skrutskie et al. 2006). Given the very rapid evolution of SN 2019neq, deep *u*, *B*, *V*, *g*, *r*, *i*, *z* template frames were observed on 2020 June 12 (MJD = 59012, only 281 rest-frame days after the maximum luminosity) by NUTS2. Since the SN was not detected in the template frames within a 3σ detection limit, we assumed that the luminosity of SN 2019neq faded well below the galaxy luminosity. Finally, it was not possible to template subtract the *J*, *H*, K_s-filter frames since no suitable template was available for these filters. Therefore we estimated the background contribution fitting a low-order polynomial. We also include *o* and *c* ATLAS (Asteroid Terrestrial-impact Last Alert System; Tonry et al. 2018a) photometry, which we converted to standard *g* and *r* via Tonry et al. (2018b). The results of our magnitude measurements are listed in Tables C1, C2, C3, and C4. Finally, we applied to these data the S- and K- corrections to bring back the many instrumental photometric systems to the corresponding standard and rest-frame ones (see Appendix A for details).

2.2 Observed and bolometric light curves

The S-corrected LCs are shown in Fig. 1. To investigate the presence of a possible pre-maximum bump feature in the LC, and to better constrain the rising phase towards the maximum luminosity, we added publicly available ZTF *g*- and *r*-filter photometry. The latest non-detection fainter than the polynomial fit of the early *g* LC corresponds to 2019 August 7 (MJD = 58703.312, *g* = 20.7 mag), and the first detection in *g* filter (*g* = 20.4 mag) was about one day later (MJD = 58704.307). It is therefore possible to estimate that the explosion date occurred on MJD $\simeq$ 58704 $\pm$ 1 (2019 August 9). Early *g*-filter detection limits exclude the occurrence of a pre-maximum bump within ~79 d before the estimated explosion date. To estimate the maximum-luminosity epoch, we fitted a high-order polynomial to the *g*-filter LC and find that the maximum occurred on $\mathrm{MJD_{MAX}} = 58731 \pm 2$ (2019 September 5) at a magnitude $g_{\mathrm{MAX}} = 17.07 \pm 0.10$ mag (uncertainties were established by varying the order of the fitted polynomial). Given a luminosity

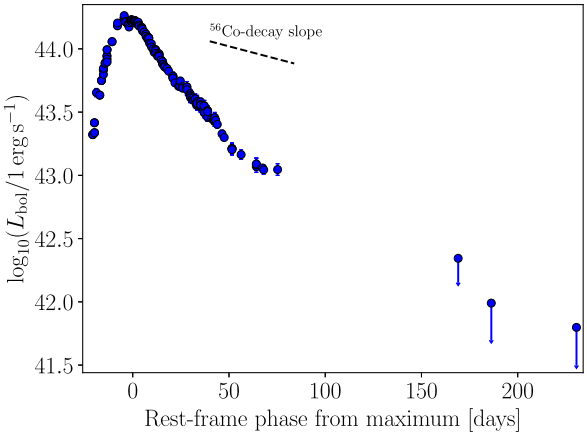

Figure 2. Pseudo-bolometric LC of SN 2019neq. For comparison also the ^{56}Co-decay slope is also shown (black-dashed line).

distance $d_{\rm L} = 482.2^{+21.3}_{-19.5}$ Mpc, corresponding to a distance modulus $\mu = 38.416^{+0.094}_{-0.090}$ mag, and a Galactic extinction $A_V = 0.104$ mag (Schlafly & Finkbeiner 2011), the peak absolute magnitude of SN 2019neq is $M_g = -21.5 \pm 0.2$ mag. As no narrow absorption lines from the Na ID doublet (Poznanski, Prochaska & Bloom 2012) are seen in the spectra, we assume no extinction from the host galaxy. In the following, we refer to the rest-frame time with respect to maximum as 'phase' (ϕ). The assumed explosion epoch implies that the phase at the point of explosion is −24 d.

The pseudo-bolometric LC of SN 2019neq was computed by integrating the broad-band photometry, adopting as reference the epochs of the *r*-filter photometry (see Fig. 2, Table C10 for the K-correction and Table C11 for the pseudo-bolometric LC). SN2019neq rises towards the maximum luminosity very rapidly at a rate $v_{\rm rise} \approx -0.13$ mag d^{-1}, it reaches a maximum luminosity of $(2.04 \pm 0.04) \times 10^{44}$ erg s^{-1} and fades at a rate $v_{\rm decline} \approx 0.05$ mag d^{-1}, which is ∼2.6 times slower than the rising rate. This ratio is somewhat higher than the typical $v_{\rm decline}/v_{\rm rise} \approx 2$ ratio for SLSNe I (Nicholl et al. 2015a).

2.3 LC bumps in SN 2019neq

LCs of SLSNe I often display pre-maximum and/or post-maximum bumps, which are usually interpreted as signatures of CSM-interaction. Their occurrence seems to be more common for the slower-evolving events (see e.g. Nicholl et al. 2015b, 2016b; Yan et al. 2015; Yan et al. 2017), but this connection is debated and might simply be due to the fact that slow SLSNe I can be observed for a longer time.

Hosseinzadeh et al. (2022) and Chen et al. (2023b) noticed post- and pre-maximum undulations in the SN 2019neq LCs respectively, and included it in sample studies of bumpy SLSNe I. In particular, Hosseinzadeh et al. (2022) used ZTF, Pan-STARRS, and ATLAS data, together with *g*, *r*, *i* observations from the 1.2 m telescope + KeplerCam at the Fred Lawrence Whipple Observatory for SN 2019neq (Szentgyorgyi et al. 2005). Their bumpy-SLSNe I sample consists of 34 objects whose LCs deviate from the best-fitting magnetar-powered MOSFIT LC, which introduces a model dependence in the definition of a 'bump'. Their KeplerCam *g*, *r*, *i* measurements are in good agreement with our coeval photometric data, which indeed seem to show a flattening at about 80 d after maximum (see Fig. 1, upper-right panel) and reveal $\lesssim 0.3$ mag-amplitude undulations occurring on a time-scale of $\lesssim 2$ d. However, given the interruption of the follow-up at this phase, we are not able to reach a firm conclusion on the veracity of physical origin of these LC features.

Chen et al. (2023b) discussed ZTF photometry which we also use in this work. In the pre-maximum data (at a phase of ∼−20), the *g* and possibly *r* LCs appear to display a hump (see Fig. 1, lower-right panel). This deviation from the general rising slope of the LCs is however encompassed by the errorbars, although the possible correspondence two bands (the only in which we have very early detections) might provide some additional support. However, as evidence for the presence of bumps is relatively weak, we do not consider data from Hosseinzadeh et al. (2022) in the following analysis.

3 SPECTROSCOPY

3.1 Observations and data reductions

Optical spectra of SN 2019neq were obtained with the 1.82m Copernico+AFOSC telescope, with NOT+ALFOSC via NUTS2, with the Xinglong 2.16-m telescope+BFOSC and with the 10.4m Gran Telescopio CANARIAS (GTC) + OSIRIS (Optical System for Imaging and low-Intermediate-Resolution Integrated Spectroscopy; Cepa et al. 2000). The raw 2D spectroscopic frames were pre-processed, wavelength-calibrated, extracted, and flux-calibrated with standard IRAF procedures called via the graphical user interface[4] FOSCGUI.[5] BFOSC spectra were reduced with IRAF procedures directly. The flux calibration of each spectrum was then checked against the coeval optical photometry (which was interpolated in case of missing epochs).

3.2 The spectra

The spectral evolution of SN 2019neq is shown in Fig. 3 (see also Table C12). Pre-maximum/maximum spectra of SN 2019neq have a hot blue continuum with blackbody temperatures of about $T_{\rm BB} \approx 16000$ K. The hot continuum is almost featureless, with only a W-shaped O II absorption feature and the O I λ 7774 feature visible in the red part. At bluer wavelengths, the Ca II H&K doublet is also present. After 10 d from maximum, the continuum cools, the W-shaped features gradually disappear in favour of the Fe II and Mg II features and the spectra of SN 2019neq start to resemble a SN Ic BL spectrum at maximum luminosity. In addition, at this phase Si II was identified by Könyves-Tóth et al. (2020) with a spectral fit obtained with SYN+ + . After +19 d, the continuum gradually cools down, and up to +80 d the spectral features do not evolve significantly, except for their intensity and velocity (see Section 4.3). At late phases, when the forbidden emission lines start to be seen in the spectrum, the Mg II feature is expected to be contaminated or replaced by the semiforbidden Mg I] λ 4571 feature; however, this region is not covered by the latest spectrum (+231 d). Finally, we used the positions of the narrow H α, [O III] host-galaxy emission lines measured in the +68, +80, and +231 d spectra to derive a host galaxy redshift of $z = 0.10592 \pm 0.00005$ (where the uncertainty is given by the dispersion of the measurements).

[4] http://sngroup.oapd.inaf.it/.

[5] FOSCGUI is a PYTHON/PYRAF based graphic user interface aimed at extracting SN spectroscopy and photometry obtained with FOSC-like instruments. It was developed by E. Cappellaro. A package description can be found at http://sngroup.oapd.inaf.it/foscgui.html.

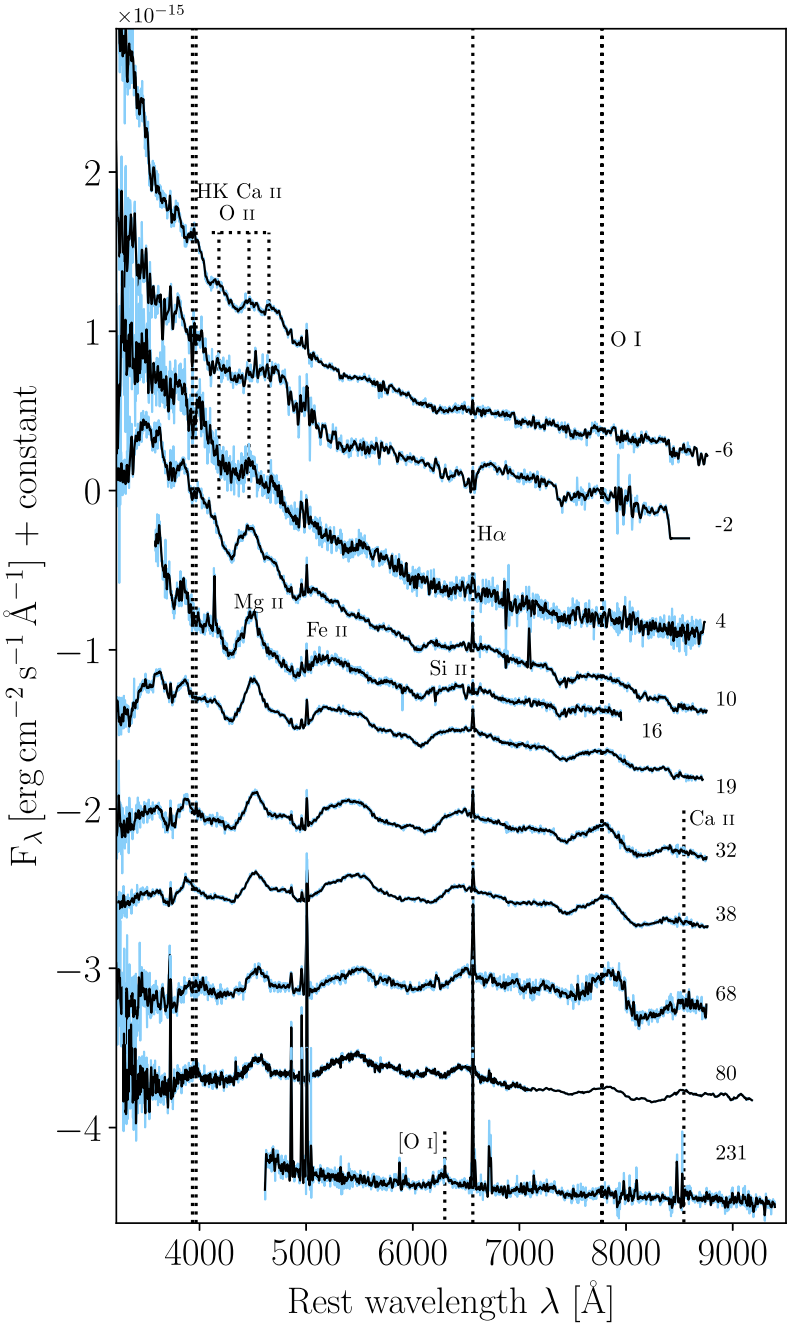

Figure 3. The spectral evolution of SN 2019neq reported to the rest-frame. The spectra (in background) were also smoothed with a Savitzky–Golay filter (Savitzky & Golay 1964, overimposed) to make the features more distinguishable. Spectra were offset and scaled. Identified spectral features are marked with black dashed lines at their corresponding rest-frame wavelength. Numbers on the right-hand side of each spectrum indicate their phase.

We also estimated the metallicity at the site of SN 2019neq by means of the narrow emission lines from the host galaxy which show up at late/nebular phases. We measured the flux emitted within these lines after optimizing the extraction from the 2D spectrum for the host-galaxy and calibrating it against the host photometry at the SN location (see also Lunnan et al. 2014). To derive the metallicity, we used the tool PYMCZ (Bianco et al. 2016). In short, PYMCZ computes the metallicity from the flux measurements of those narrow emission lines via a number of metallicity diagnostics. To associate the errorbars to the metallicity measurements, PYMCZ randomly samples a Gaussian distribution whose mean and standard deviation are given by the flux measurements and their uncertainties, respectively. In the case of SN 2019neq, we measured the flux emitted within the [O II] λ 3727, H β, [O III] λ 4959, [O III] λ 5007, H α, [S II] λ 6717 emission lines. The nebular spectrum of SN 2019neq at 231 d after maximum does not show the [N II] λλ 6548, 6583 narrow emission lines. The only diagnostic which could be suitably used is then the M08_O3O2 (Maiolino et al. 2008), giving a metallicity $12 + \log_{10}(\mathrm{O/H}) \simeq 8.3$, which corresponds to $Z \simeq 0.4\,Z_{\odot}$ assuming a solar metallicity $12 + \log_{10}(\mathrm{O/H}) = 8.69$ (Asplund et al. 2009).

Finally, we estimated the star formation rate (SFR) of the host galaxy of SN 2019neq based on the measurements of the flux

emitted by the reddening corrected narrow H α using equation (2) of Kennicutt (1998). The derived SFR is $\simeq 2.6\,M_{\odot}\,yr^{-1}$, similar to the SFRs measured by Chen et al. (2017) for a sample of galaxies hosting SLSNe I. In addition, we estimated the specific SFR, i.e. the SFR expressed per unit of stellar mass content of the host galaxy, sSFR $\equiv$ SFR/M_*. To estimate M_*, we used equation (8) of Taylor et al. (2011) after having measured the $g_{host} = 20.4 \pm 0.1$ mag and $i_{host} = 19.7 \pm 0.1$ mag for the host galaxy. We adopted Galactic extinction corrections from Schlafly & Finkbeiner (2011) and we obtained K-corrections scaling a starburst-galaxy template from Calzetti, Kinney & Storchi-Bergmann (1994) to the g_{host} and i_{host} magnitudes, thus obtaining $\log_{10}M_*/M_{\odot} \simeq 9.1$ and sSFR $\simeq 2.3\,Gyr^{-1}$. These values are in a good agreement with the average properties of a sample of 31 SLSNe I host galaxies studied by Lunnan et al. (2014). We stress that the SFR and sSFR values deduced can be highly affected by the error on the K-corrections.

4 DISCUSSION

4.1 Photometric and spectroscopic comparisons

In order to highlight its similarities/differences with other SLSNe I, we selected a sample including both very slow- and fast-evolving SLSNe I to compare their K-corrected g-filter absolute LCs and spectra with those of SN 2019neq. The slow-SLSNe I subsample consists of SN 2020wnt (Gutiérrez et al. 2022), SN 2015bn (Nicholl et al. 2016a), and PTF12dam (Nicholl et al. 2013; Chen et al. 2015; Vreeswijk et al. 2017), while the fast-SLSNe I one includes SN 2011ke and PTF11rks (Inserra et al. 2013; Quimby et al. 2018). In addition, we imported the best-sampled and non-heavily oscillating g-filter ZTF LCs among those published in Chen et al. (2023a) (see Table 1). We compared the LCs of the SLSNe I of this sample with that of SN 2019neq. In addition, we investigated if SN 2019neq has a peculiar behaviour compared to the expected correlation between the SLSNe I maximum luminosity and the evolutionary time-scales (see Inserra et al. 2018).

The LC comparison was done both in absolute and normalized units (see Fig. 4, left and right panel, respectively). When the K-corrections were not available from the spectra, we approximate it as $-2.5\log_{10}(1+z)$ (Hogg et al. 2002), which was shown to be a reasonable approximation for SLSNe I (Chen et al. 2023a). The LCs of the ZTF subsample are coloured according to their evolutionary velocity: we used the normalized magnitude at a phase of -15 rest-frame days, $g_{norm,-15}$, as a proxy for it. Hence, faster-evolving SLSNe I have greater values of $g_{norm,-15}$ and vice versa. To measure $g_{norm,-15}$, for each SN we fitted a polynomial to the g-filter

Table 1. The SLSNe I sample used in this work (including SN 2019neq) with the values of $g_{norm,-15}$ and g_{max} and the reference used for the data (errors in parenthesis). Absolute magnitudes in AB system, corrected for foreground extinction and K-corrected, and referred to the cosmological model assumed in this work.

Name	$g_{norm,-15}$	g_{max}	Reference
SN2018bym	0.26(0.05)	−21.88(0.02)	Chen et al. (2023a)
SN2018fcg	1.55(0.05)	−20.32(0.05)	Chen et al. (2023a)
SN2018kyt	1.73(0.00)	−20.68(0.07)	Chen et al. (2023a)
SN2019cdt	0.74(0.01)	−21.07(0.07)	Chen et al. (2023a)
SN2019aamp	0.20(0.04)	−22.14(0.02)	Chen et al. (2023a)
SN2019kwt	0.38(0.07)	−22.57(0.02)	Chen et al. (2023a)
SN2019eot	0.17(0.07)	−22.43(0.03)	Chen et al. (2023a)
SN2019lsq	0.54(0.05)	−20.68(0.03)	Chen et al. (2023a)
SN2019nhs	0.36(0.05)	−21.48(0.02)	Chen et al. (2023a)
SN2019stc	0.43(0.01)	−20.39(0.03)	Chen et al. (2023a)
SN2019unb	0.18(0.08)	−19.91(0.08)	Chen et al. (2023a)
SN2019ujb	0.25(0.10)	−21.42(0.08)	Chen et al. (2023a)
SN2019zbv	0.36(0.07)	−21.99(0.03)	Chen et al. (2023a)
SN2020fvm	0.29(0.05)	−21.43(0.06)	Chen et al. (2023a)
SN2020auv	0.35(0.06)	−21.72(0.05)	Chen et al. (2023a)
SN2020exj	0.91(0.03)	−20.48(0.02)	Chen et al. (2023a)
SN2020htd	0.34(0.10)	−21.39(0.02)	Chen et al. (2023a)
SN2019neq	1.10(0.13)	−21.62(0.20)	this work
SN2010gx	1.16(0.02)	−20.91(0.20)	Pastorello et al. (2010)
PTF11rks	4.41(0.02)	−21.00(0.05)	Inserra et al. (2013)
SN2015bn	0.07(0.05)	−22.17(0.04)	Nicholl et al. (2016a)
PTF12dam	0.08(0.07)	−21.79(0.10)	Nicholl et al. (2013)
SN2011ke	0.28(0.03)	−21.60(0.05)	Inserra et al. (2013)
SN2020wnt	0.09(0.03)	−20.44(0.03)	Gutiérrez et al. (2022)

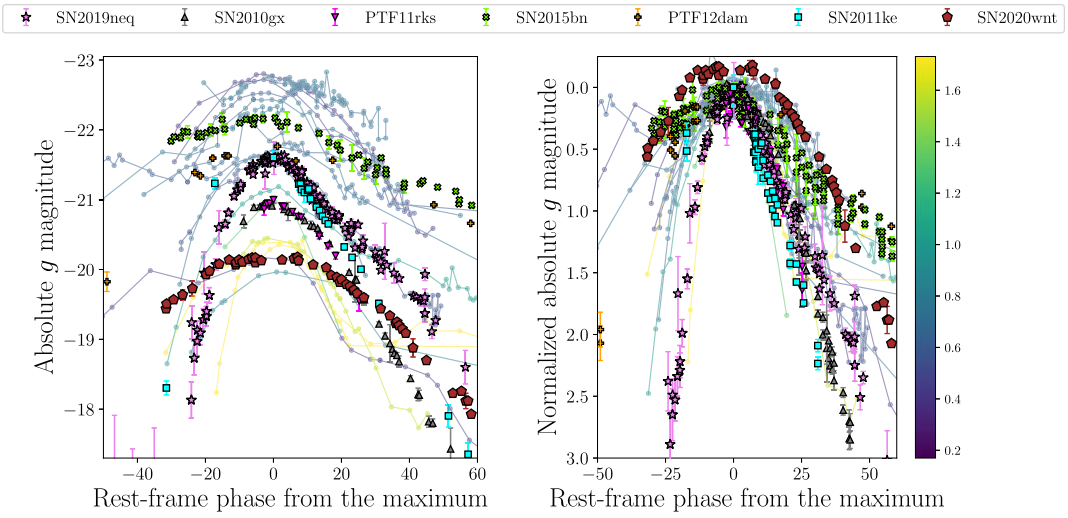

Figure 4. Comparisons of the absolute g-filter LC of SN 2019neq (stars) with those of two fast-evolving SLSNe I, SN 2011ke (squares) and PTF11rks (inverted triangles) (data from Inserra et al. 2013) and two slow-evolving SLSNe I, SN 2015bn (crosses) (Nicholl et al. 2016a) and PTF12dam (plus symbols) (Nicholl et al. 2013; Chen et al. 2015; Vreeswijk et al. 2017). Right panel: LCs comparison normalized to the same maximum luminosity. Left panel: LCs comparison without rescaling. The absolute LCs were computed assuming the cosmological parameters used in this work (see the Introduction).

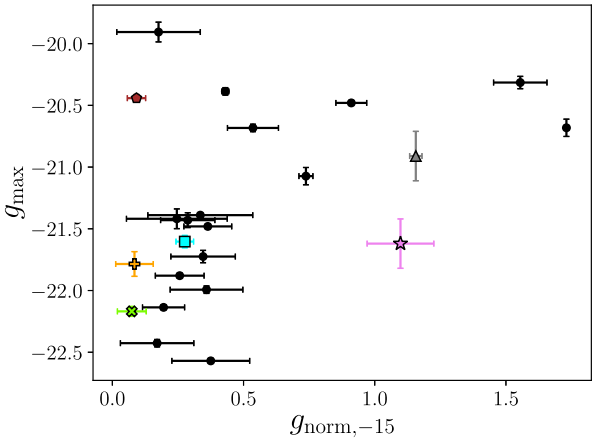

Figure 5. Absolute g-filer magnitude g_{max} (corrected for foreground extinction and K-corrected) versus the normalized magnitude at −15 d $g_{norm,\,-15}$ (see the text). Black dots correspond to the ZTF sample (see Table 1 for the coordinates), while the other symbols are the same as in Fig. 4.

LC around the maximum luminosity. The degree of the polynomial and the fit domain were varied in order to minimize the root-mean squared of the fit. This quantity was also used as errorbar on $g_{norm,\,-15}$, although this choice may overestimate it. The values of $g_{norm,\,-15}$ and g_{max} of the selected comparison sample are listed in Table 1 too. We then plot the g_{max} values versus $g_{norm,\,-15}$ (Fig. 5). Our sample confirms the abovementioned correlation between peak luminosities and the evolutionary time-scales, with some exceptions none the less: SN 2019neq is actually one of the outliers as it evolves faster than the other SLSNe I with comparable peak luminosities; SN2018bym and the peculiar SN 2020wnt are slower than the other SLSNe I having comparable peak luminosities. On the contrary, SN 2015bn, PTF12dam, SN 2010gx, and SN 2011ke better agree with the general trend followed by the ZTF subsample (PTF11rks was excluded due to the lack of pre-maximum data). However, much larger samples are required to draw general conclusions on this.

Furthermore, we compared three spectra of SN 2019neq (at phases −6, +10, + 231 d) with the available spectra for the comparison sample (including some of those belonging to the ZTF sample, see Fig. 6) at similar phases. In particular, we included pre-maximum spectra of SN 2019nhs and SN 2019unb and post-maximum spectrum of SN 2019cdt. We also added a spectrum of the type-Ic BL SN 2003jd at about its maximum luminosity given its resemblance to SLSNe I spectra after maximum (see Section 1). The absorptions on the blue part of the early spectrum of SN 2019neq are different from those of SN 2015bn, PTF11rks, and SN 2020wnt, and hence due to other transitions (see also Könyves-Tóth & Vinkó 2021), while they possibly share the broad features from Si II and O II on the red side. In particular, the spectrum of SN 2019neq at −6 d looks more similar to the almost coeval one of SN 2019unb, whose location in the ($g_{norm,\,-15}$, g_{max}) space is also peculiar (see Table 1). At later phases, the spectrum of SN 2019neq (+10 d after maximum) is similar to that of PTF11rks at the same phase and shows several broad features which nearly reproduce the spectral behaviour of SNe Ic BL at maximum luminosity. To see this, we compared the spectrum of SN 2019neq at 10 d after maximum with that of the SN 2003jd at maximum luminosity, which was given as best-match template by GELATO (Harutyunyan et al. 2008). Also the post-maximum spectrum of SN 2020wnt, PTF12dam, and SN 2019cdt are similar to the other spectra shown at comparable phases, but the prominent feature seen in these spectra at about 4700 Å cannot be easily explained by the Mg II λ4571 only. Finally, the spectrum of SN 2019neq observed 231 d after maximum was compared with the spectra of PTF12dam and SN 2020wnt. At these epochs, the spectra look different. In particular, the nebular spectra of PTF12dam and SN 2020wnt still show some broad features between 5000 and 6000 Å and more prominent [Ca II] λλ 7291, 7323 and O I λ 7774 features. The nebular spectrum of SN 2019neq looks instead pretty much featureless, except for the [O I] λλ 6300,6364; however, its lower signal-to-noise ratio makes a more thorough comparison difficult.

4.2 SED, colours, photospheric temperature, and radius evolutions

We discuss the SED evolution by analysing the time variation of properties deduced from the multicolour photometry presented in Section 2. In detail, we present the rest-frame colours (Figs 7 and 8), photospheric temperature and radius evolution. Photospheric temperatures were estimated by fitting a blackbody curve to the SED and the photospheric radius was inferred via the Stefan–Boltzmann law. To exclude any possible UV/NIR deviations from the blackbody, we repeated the calculation excluding the $uvw2$, $uvm2$, $uvw1$, J, H, K_s-fluxes from the SED (Figs 9 and 10). In addition, for each epoch $t = \phi$ + 24 (hence the phase from explosion, assuming an explosion phase of −24 d, see Section 2.2) we estimated the photospheric temperature and radius from spectra: to do this, we fitted blackbody curve to spectra and computed for each epoch t the radius as $v_{phot}(t) \times t$ (see Dessart et al. 2015, and discussion in Section 4.3). However, we found no major temperature differences between the three estimates and conclude that, at least at photospheric post-maximum phases (see later), the SED is reasonably well described by a blackbody over UV/optical/NIR wavelengths.

We compare the colour evolution of SN 2019neq with other SLSNe I with different evolutionary time-scales. After the initial nearly constant phase, the colours of SN 2019neq rapidly evolve towards red similar to the fastest-evolving SLSNe I of this sample (see e.g. PTF11rks, SN 2010gx and SN 2020ank; Pastorello et al. 2010; Inserra et al. 2013; Kumar et al. 2020). In contrast, colours of slower evolving SLSNe I redden at a slower pace compared to the fastest ones; the behaviour of SN 2017gci is odd, but its atypical colour evolution is likely ascribable to the ∼0.6-mag-wide bumps in its LC (Fiore et al. 2021). However, in all cases SLSNe I display blue colours around the pre-maximum/early-post-maximum phases (Pastorello et al. 2010; Chomiuk et al. 2011; Quimby et al. 2011; Leloudas et al. 2012; Inserra et al. 2013). In particular, at this phase the rest-frame $g - r$ colour remains almost constant at ∼− 0.25 mag for every SLSNe I considered in Fig. 7; which likely means that the SED does not significantly evolve. This is true also for SN 2019neq: to verify whether this behaviour is seen in other colour indexes, we extend the time coverage of the observed photometry by performing synthetic photometry on the spectra (see dotted lines in Fig. 8), this is particularly useful in u band (although the flux calibration of the spectra is less precise and synthetic-photometry measurements are in part extrapolated, see Fig. 8, right panel). As can be seen in Fig. 8, the initial flattening appears present in $u - g$ and $g - z$ too, although very early photometric measurements can be done only in g and r filters. Subsequently, we see that after ∼30–40 d from the maximum luminosity the $g - r$ colour curve flattens again.

The nearly constant initial behaviour of the colour could reflect the early photospheric-temperature evolution; however, due to the lack of UV data at pre-maximum phases, the initial plateau phase cannot be fully trusted. Soon after maximum, the photospheric temperature

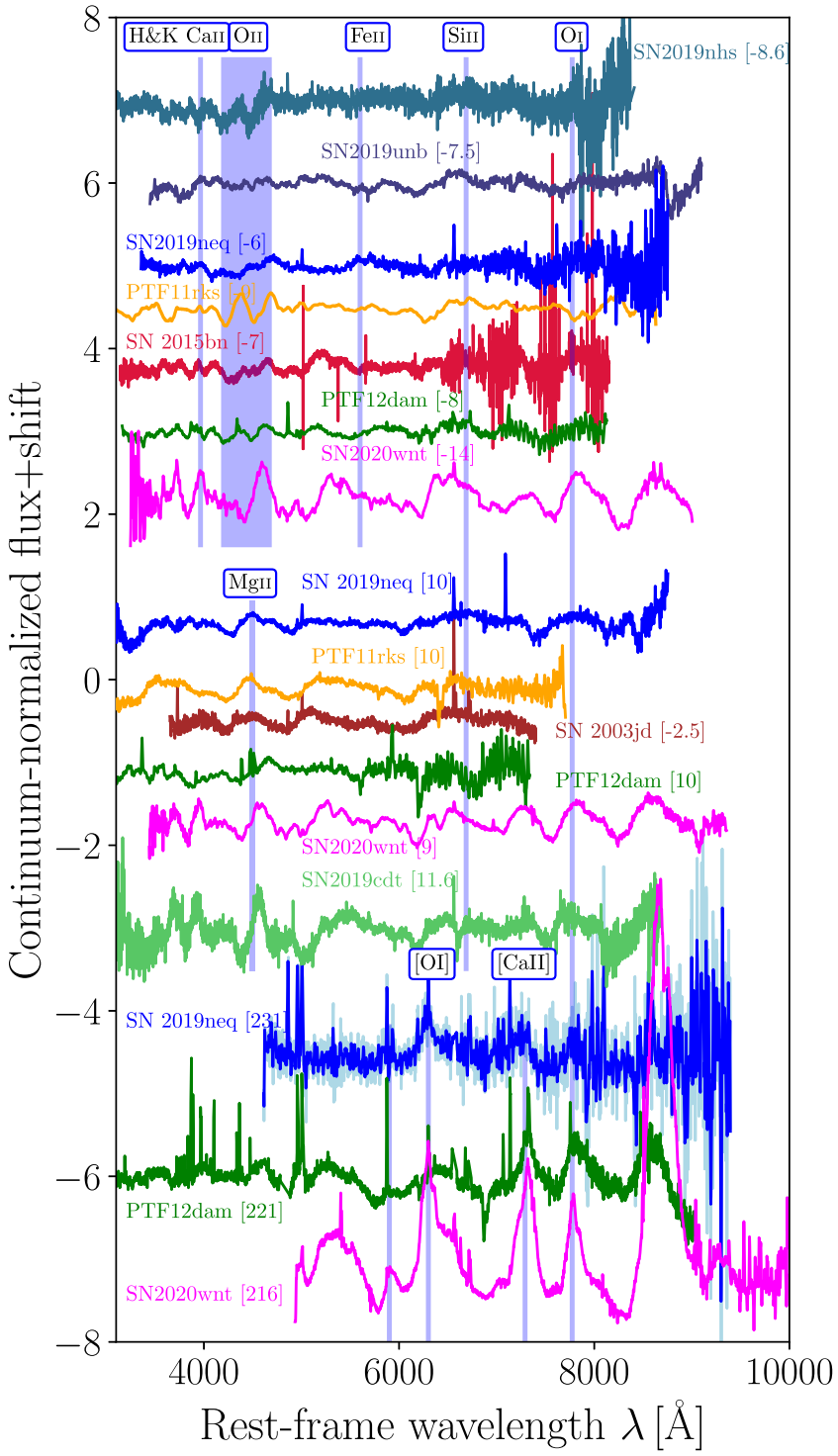

Figure 6. Comparison of three spectra of SN 2019neq with those of other SLSNe at broadly coeval phases with respect to maximum. The phases are reported in square brackets. Line identifications are marked with blue shaded areas and for each of them the corresponding ion is labelled on the top. For the last spectrum of SN 2019neq (+231 days) we plot both the original and its smoothed version (with a Savitzky-Golay filter, plotted in background).

starts to decline, reaching a new constant value after ∼30 d (similar to other SLSNe I, see also Nicholl, Guillochon & Berger 2017). Interestingly, at comparable phases, the photospheric radius reaches a maximum (Fig. 10) and then starts to recede: a similar trend of the photospheric-radius evolution is described by a simple model (Liu et al. 2018) assuming homologous expansion and constant opacity. However, more detailed calculations of the photospheric radius with a proper time-varying opacity are needed to constrain the ejecta-density profile of SN 2019neq, and this will be the subject of future investigations.

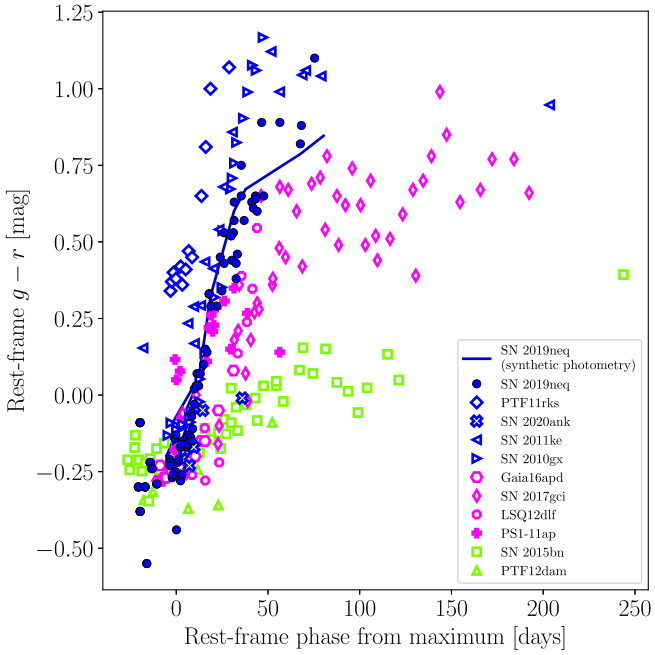

Figure 7. Rest-frame $g - r$ evolution of SN 2019neq (blue filled dots) compared to that of a sample of fast-evolving (blue-edged markers), intermediate (magenta-edged markers), and slow-evolving SLSNe I (green-edged markers). The solid-blue line joins the rest-frame $g - r$ points computed via synthetic photometry on the spectra of SN 2019neq. A color version of the figure is available in the online version.

4.3 Photospheric velocity

To estimate the photospheric velocity of SN 2019neq, the minima of the O I λ 7774 P-Cygni profiles were measured with a Gaussian fit (see Fig. 11) after having normalized and continuum-subtracted the spectra. These measurements were performed on the spectra at phases −6 to 80 d with respect to the maximum luminosity. By measuring the Doppler shift compared to the rest-frame wavelength of the corresponding maximum, we obtained the expansion velocity. This was used as a proxy for the photospheric velocity (Dessart et al. 2015) (see Fig. 12). Errorbars were estimated by changing the continuum level multiple times before performing the fit. The comparison between the radii deduced from photometry and spectroscopy confirms that the O I is a good tracer of the photosphere for SN 2019neq for ϕ between ∼−5 and 18 d, where we inferred an average photospheric velocity of ∼ 12500 km s^{-1}. Overall, the Doppler shift measured with respect to the rest-frame wavelength of the emissions corresponds to a photospheric velocity v(O I) ≈ 12500 − 15000 km s^{-1}. We also compared the photospheric velocities of SN 2019neq with those of other SLSNe I whose velocity measurements are available in literature: iPTF13ehe (Yan et al. 2015), iPTF15esb (Yan et al. 2017), SN 2015bn (Nicholl et al. 2016a), SN 2017gci (Fiore et al. 2021), and SN 2018hti (Lin et al. 2020; Fiore et al. 2022). In addition, given the unusually high velocities of SN 2019neq, we included in the comparison sample also two SNe Ic BL, namely SN 2003jd (Valenti et al. 2008) and SN 2007ru (Sahu et al. 2009) (see Fig. 12). The high velocities of SN 2019neq do not seem to be correlated with a steeper average velocity gradient compared to slower SLSNe I (like SN 2015bn or SN 2018hti), as suggested by Inserra et al. (2018) and Könyves-Tóth & Vinkó (2021), whereas this remains true for iPTF13ehe and iPTF15esb. The same appears to be also valid for the SNe Ic BL SN 2007ru and SN 2003jd, the latter reaching even higher velocities at maximum epochs. We notice that the velocities of SN 2019neq deduced by us are in tension with those deduced by Könyves-Tóth & Vinkó (2021), who measure $v_{\rm phot} \simeq 23000$ km s^{-1} at $\phi = -4$ d. However, Könyves-Tóth & Vinkó (2021) used a different method to infer the $v_{\rm phot}$ values: they cross-correlated the observed spectra of SN 2019neq with a template SYN++ spectrum computed with $v_{\rm phot} = 10000$ km s^{-1} and found a velocity difference $\Delta v_{\rm X}$. The $\Delta v_{\rm X}$ values were then used to obtain the $v_{\rm phot}$ measurements after having applied a correction (see Section 4.1 and equations 10, 11 in Könyves-Tóth & Vinkó 2021).

4.4 Modelling SN 2019neq

We used the nebular spectrum of SN 2019neq at 231 d to infer an estimate of the mass of the oxygen zone of the ejecta. The absolute integrated luminosity emitted within the O I λ 7774 feature can be used to infer the O-zone mass (see equations 7,8 of Jerkstrand et al. 2017). In addition, we used the SUMO models for the nebular spectra[6] of SNe Ic (Jerkstrand et al. 2017). The broad constraint obtained on the ejecta mass will be used in Section 4.4.2 as prior to favour one of the possible best-fitting bolometric LCs obtained with the MOSFIT (Guillochon et al. 2017a, b) tool. For this same SN, Könyves-Tóth et al. (2020) estimated an ejecta mass of ∼ 23 M$_\odot$ assuming an ejecta opacity $\kappa = 0.1$ cm^2 g^{-1}. In the following, we will more carefully investigate this comparing the photometric best-fitting value with the analysis of nebular spectroscopy.

4.4.1 Nebular-spectrum modelling

The SUMO nebular spectra are single-zone models computed for three different compositions (pure-O, C-burning ashes and OMg). For each composition, spectra calculations assume a phase of 400 d after the explosion, the homologous expansion of the ejecta at a constant velocity $V = 8000$ km s^{-1} and $N = 100$ random clumps for different ejecta masses[7] $M_{\rm ejecta}^{\rm SUMO} = 3, 10, 30$, energy deposition $E_{\rm dep} = 2.5 \times 10^{41} - 2 \times 10^{42}$ erg s^{-1}, and filling factors $f = 0.1, 0.01, 0.001$. The filling factor expresses the percentage volume of clumps, hence lower f values correspond to more clumped ejecta.

Before measuring the O I λ 7774 absolute luminosity, we estimated the residual contribution of the host-galaxy emission using the host-galaxy spectrum adjacent to that of SN 2019neq. Then this was scaled and subtracted from the spectrum of SN 2019neq until the narrow galaxy emission was removed from the SN spectrum. Then, we measured an integrated luminosity of the O I λ 7774 line of $L_{7774} \lesssim 2 \times 10^{40}$ erg s^{-1}. Due to the relatively low signal-to-noise ratio between 7000 and 8000 Å, we assume this value as an upper limit. Similar to the SUMO models, we assumed a maximum velocity of the fluid elements $V = 8000$ km s^{-1}. Aside this parameter, the only tunable quantities are the clumping factor f and the electron fraction x_e. We computed the O-zone mass for the f values with which SUMO models are computed, i.e. $f = 0.1, 0.01, 0.001$, a phase from the explosion of 231 + 24 d = 255 d (see Section 2.2) and we consider a range of $x_e = 0.05 - 0.1$ (this range encompasses the typical values used in SUMO models; Jerkstrand et al. 2017). Results are shown in Table 2. The case $f = 0.1$ leads to very high O-zone masses ($M(O) > 100$ M$_\odot$): based on the rapid LC-evolution time-scales, in the following we will not consider this case anymore. The $f = 0.01, 0.001$ cases allow for lower O-zone

[6] https://zenodo.org/records/5578729.

[7] In the following, we will refer to the ejecta mass in unit of solar masses with which SUMO models are computed as $M_{\rm ejecta}^{\rm SUMO}$ to distinguish them from other ejecta-mass estimates.

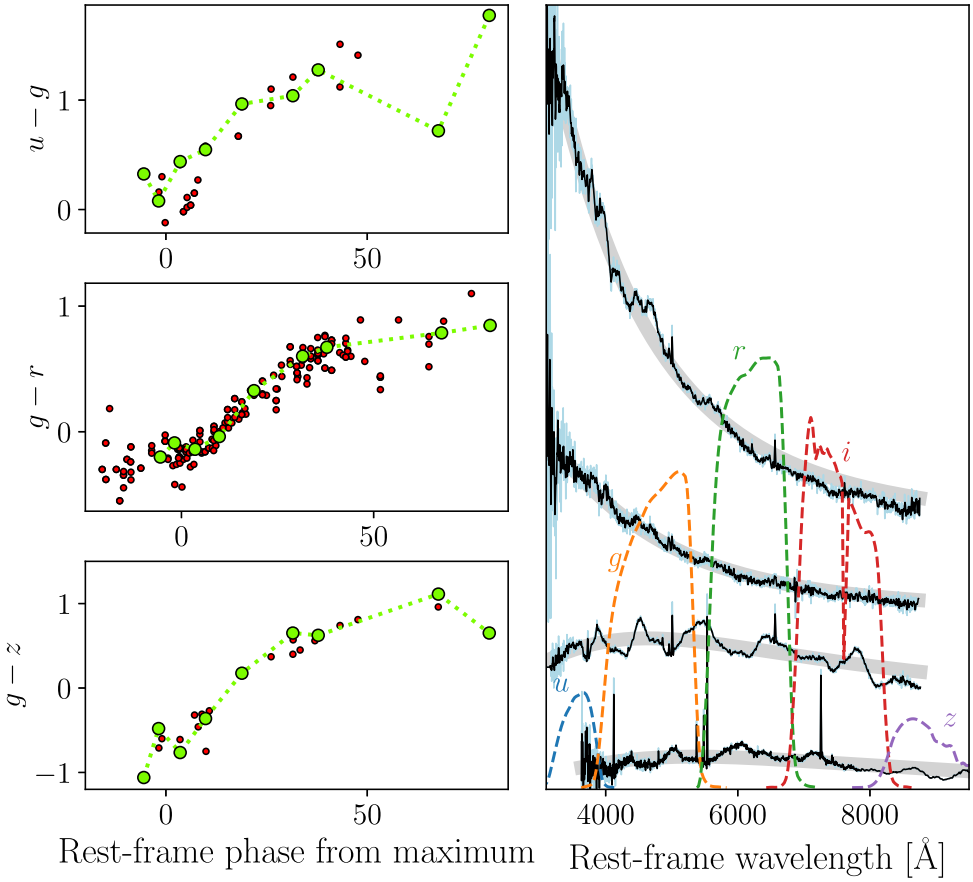

Figure 8. Left panels: rest-frame colour evolution of SN 2019neq (little dots are photometric points and big dots are obtained from synthetic photometry on the observed spectra). Right panel: four representative spectra of SN 2019neq (see Fig. 3) within ∼80 d from the maximum luminosity. The dashed curves represent the throughput of the *u*, *g*, *r*, *i*, and *z*-passband filters.

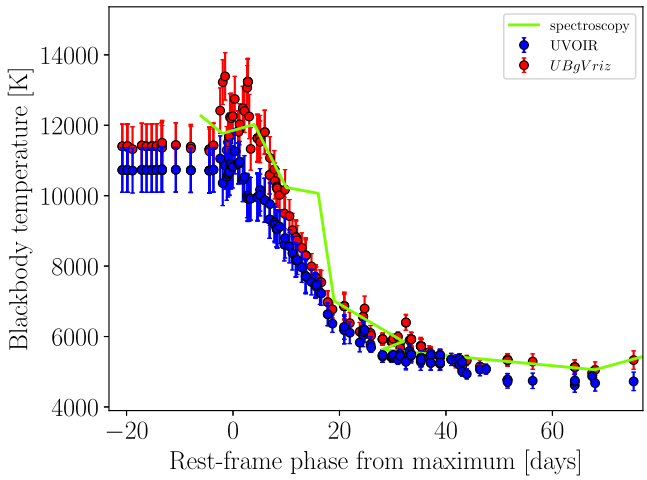

Figure 9. Evolution of the photospheric temperature. Blue dots represent values obtained integrating over the entire set of multiband photometry available, while red dots were obtained using only the *UBgVriz* bands. The green line represents the evolution of the photospheric temperature obtained from a blackbody fit to the spectra. A color version of the figure is available in the online version. A color version of the figure is available in the online version.

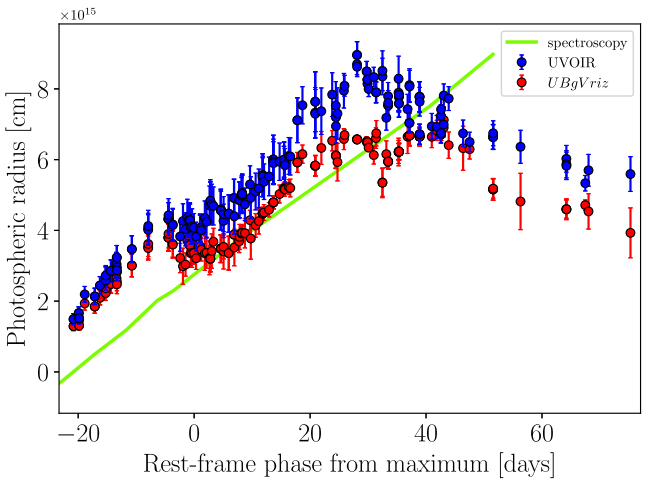

Figure 10. Evolution of the photospheric radius. Dots are colour-coded as in Fig. 9. The green line was obtained using the photospheric velocities measured with the spectra. A color version of the figure is available in the online version.

masses permitted by lower mass ejecta. In addition, our mass estimates are strongly affected by our assumption on the electron fraction x_e, the clumping factor f, and the maximum velocity of the clumps V.

We then consider SUMO models computed for $f = 0.01, 0.001$, $M_{\rm ejecta}^{\rm SUMO} = 3, 10, 30$ for pure-Oxygen, OMg and C-burning abundances, and different values of the energy deposition $E_{\rm dep} = 2 \times 10^{41} - 2 \times 10^{42}$ erg s^{-1} (see Figs B1, B2, B3, B4, B5, and B6). [O I] seems to be better described by models with $M_{\rm ejecta}^{\rm SUMO} = 10$ and $f = 0.01$

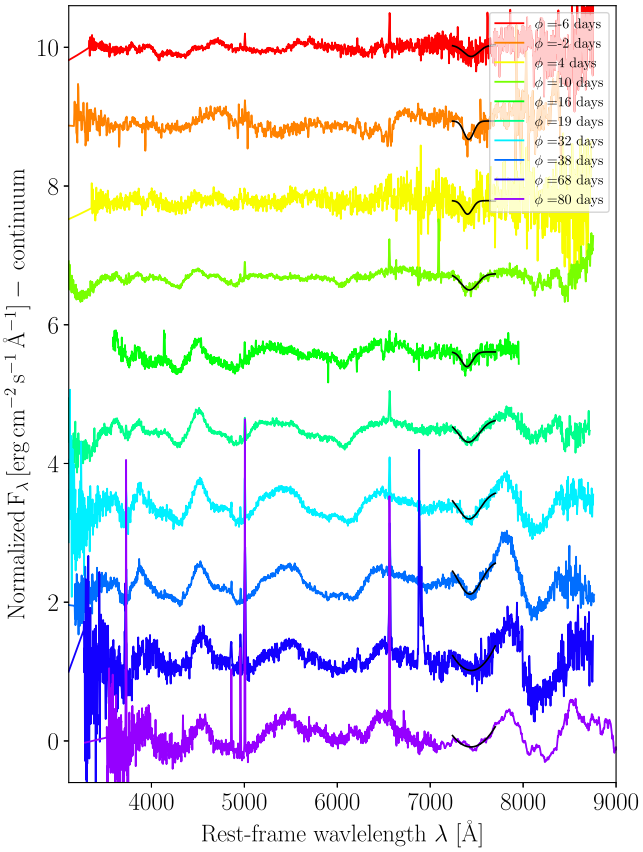

Figure 11. Normalized and continuum subtracted spectra of SN 2019neq, with the photospheric velocity being measured by fitting the minimum of the O I λ7774 absorption feature with a Gaussian (black solid lines).

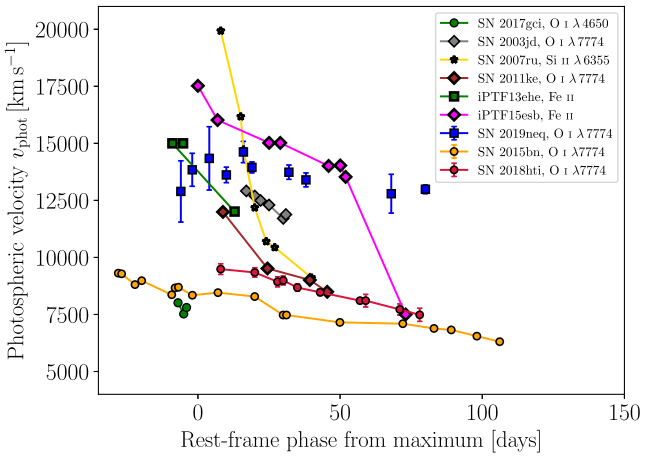

Figure 12. Photospheric velocities of SN 2019neq (blue squares) compared with those of SN 2003jd (silver diamonds; Valenti et al. 2008), SN 2007ru (yellow stars; Sahu et al. 2009), SN 2011ke (purple diamonds; Inserra et al. 2013), iPTF13ehe (green squares; Yan et al. 2015), iPTF15esb (magenta diamonds; Yan et al. 2017), SN 2015bn (orange dots; Nicholl et al. 2016a), SN 2017gci (green dots; Fiore et al. 2021), and SN 2018hti (red dots; Fiore et al. 2022). A color version of the Figure is available in the online version.

Table 2. Electron density n_e and O-zone mass $M(O)$ computed for $f = 0.1$, 0.01, 0.001 after having fixed $L_{7774} = 2 \times 10^{40}$ erg s^{-1}, $t = 255$ d (here we have assumed a rise time of 24 d, see Section 2.2) and $V = 12500$ km s^{-1}. The $M(O)$ values in parentheses are computed for $x_e = 0.1$, otherwise for $x_e = 0.05$.

f	0.1	0.01	0.001
n_e (10^8 cm^{-3})	1.3	4.1	13
$M(O)$ [M$_\odot$]	122(61)	39(19)	12(6)

for higher energy deposition, thus possibly favouring higher values of the electron fraction x_e. Other models underpredict the [O I] λ 63 006 364 feature, except the C-burning models with $M_{\rm ejecta}^{\rm SUMO} = 30$ and $E_{\rm dep} > 1 \times 10^{42}$ erg s^{-1}. Furthermore, OMg-composition models seem less suitable to explain the O I features seen in the nebular spectrum of SN 2019neq, in particular for $E_{\rm dep} = 2 \times 10^{41}$ erg s^{-1} (see Figs B5 and B6). However, the temporal discrepancy between the observed nebular spectrum of SN 2019neq and the SUMO solutions makes the SUMO spectra by a factor $(400/255)^3 \sim 3.9$ less dense than the observed, if ejecta mass and expansion velocity are the same: this makes their spectral comparisons less relevant to discriminate among the different ejecta configurations. In addition, we warn the reader that a more careful estimate of the physical parameters of SN 2019neq would need independent constraints to break some degeneracies (e.g. between n_e and f or between $E_{\rm in}$ and $M_{\rm ejecta}$); this is however beyond the scope of this work.

4.4.2 *Light-curve modelling*

We modelled the LCs of SN 2019neq to estimate the physical parameters of the explosion assuming the magnetar and the ejecta-CSM interaction. We used the Modular Open Source Fitter for Transients (MOSFIT) tool (Guillochon et al. 2017a, b) which offers a set of modules to fit the observed multicolour LCs for different kind of transients. For SN 2019neq, we ran MOSFIT using the SLSN and the CSM modules, computing synthetic LCs powered by magnetar spin-down (Kasen & Bildsten 2010; Inserra et al. 2013) and CSM (Chatzopoulos, Wheeler & Vinko 2012) interaction, respectively. We fixed $\kappa = 0.1$ cm^2 g^{-1} for both models which is suitable for SNe Ic (e.g. Nagy 2018).

The CSM fit was set up adopting a broken power-law ejecta density profile as in Chatzopoulos, Wheeler & Vinko (2012) with fixed exponents $n = 12$ and $s = 2$, suitable for a steady wind-like CSM. A shell-like CSM ($s = 0$) fit is not well constrained by the data, hence we excluded it. The $s = 0$ CSM best-fitting parameters are a CSM mass of $M_{\rm CSM} \simeq 0.7$ M$_\odot$, a progenitor radius $R_0 \simeq 1.4 \times 10^{14}$ cm, a CSM density $\rho \simeq 1.8 \times 10^{-10}$ g cm^{-3}, an ejecta mass $M_{\rm ejecta} \simeq 21.9$ M$_\odot$, an average ejecta velocity $v_{\rm ejecta} \simeq 4100$ km s^{-1} and a temperature floor $T_{\rm min} \simeq 3700$ K. This corresponds to a kinetic energy of $\sim 3.7 \times 10^{51}$ erg. The ejecta mass for the CSM fit broadly agrees with the SUMO models computed $M_{\rm ejecta}^{\rm SUMO} = 30$. The SLSN fit predicts a lower ejecta mass (~ 12 M$_\odot$), thus in better agreement with SUMO spectra with $M_{\rm ejecta}^{\rm SUMO} = 10 - 30$. This is especially true for SUMO models computed with $M_{\rm ejecta}^{\rm SUMO} = 10$ and $f = 0.01$. To verify whether higher ejecta-mass models return reasonable results, we performed another SLSN fit, this time fixing an ejecta mass $M_{\rm ejecta} = 25$ M$_\odot$ and fitting the opacity: not surprisingly, in this last case the best-fitting opacity is lower ($\kappa = 0.05$ cm^2 g^{-1}), but however reasonable in the case of H/He-poor events (Nagy 2018). Both the $\kappa = 0.05$ cm^2 g^{-1} and the $\kappa = 0.1$ cm^2 g^{-1} SLSN fits provide ejecta-mass estimates that are broadly consistent with what can be inferred via the nebular-spectrum interpretation presented in the previous section. The other best-fitting parameters for the two SLSN fits are a magnetic field $B \simeq 6 \times 10^{14}$ G, an initial spin period $P_{\rm init} \sim 1.1 - 1.5$ ms, a temperature floor $T_{\rm min} \simeq 6000$ K, and an average ejecta velocity $v_{\rm ejecta} \simeq 10000$ km s^{-1}. This

Table 3. MOSFIT CSM physical parameters (the opacity, marked with (*) is a fixed parameter; the other ones are best-fitting values).

M_{CSM} [$M_\odot$]	R_0 (10^{14} cm)	ρ (g cm^{-3})	M_{ejecta} [$M_\odot$]	κ (cm^2 g^{-1})	T_{min} (10^3 K)	v_{ejecta} (10^3 km s^{-1})
0.74	1.36	1.78e-10	21.88	0.1(*)	3.73	4.05

Table 4. MOSFIT SLSN physical parameters (the one with (*) is a fixed parameter, the other ones are best-fitting values).

B [10^{14} G]	M_{NS} [$M_\odot$]	P_{spin} (ms)	M_{ejecta} [$M_\odot$]	κ (cm^2 g^{-1})	T_{min} (10^3 K)	v_{ejecta} (10^3 km s^{-1})
5.98	1.66	1.47	11.75	0.1(*)	5.94	10.05
5.76	1.49	1.01	25(*)	0.05	5.96	10.43

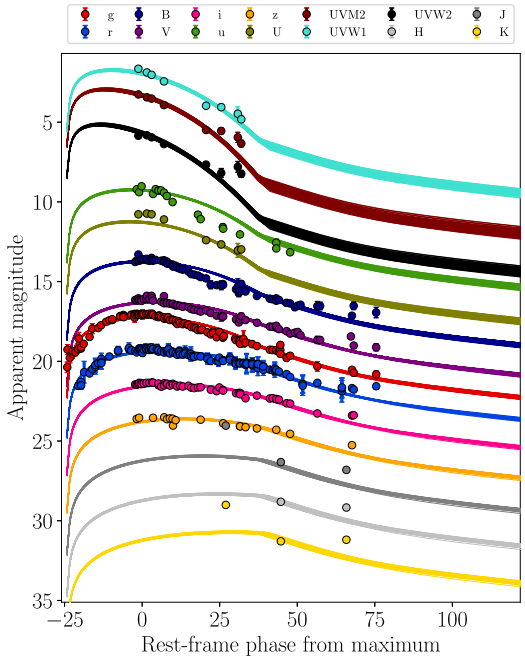

Figure 13. Multicolour synthetic LCs output by MOSFIT SLSN-model.

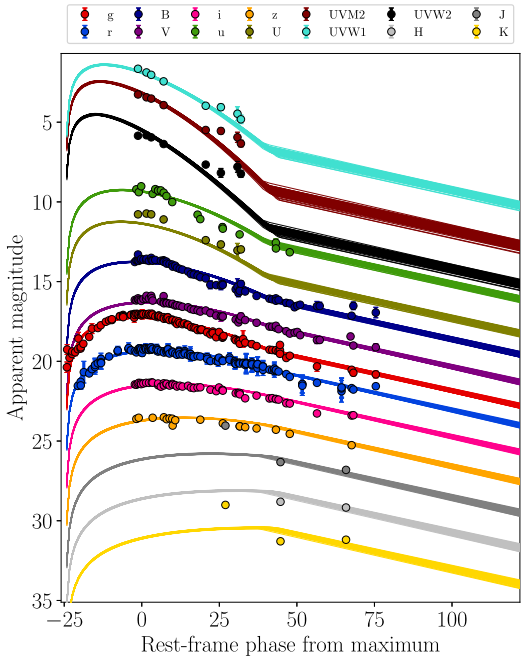

Figure 14. Same as Fig. 14, but for the CSM-model.

correspond to a kinetic energy of $1.3 - 2.7 \times 10^{52}$ erg. The best-fitting parameters for the CSM and SLSN are listed in Tables 3 and 4 and the corner plots showing their posterior distributions are shown in Figs B7 and B8, respectively. The SLSN and CSM LCs are shown in Figs 13 and 14 and are able to capture the pre-maximum/maximum luminosity epochs. The early post-maximum photometric detections in *uvm*2 and *uvw*2 bands cannot be properly described by both models; moreover, red and NIR-bands photometric points at a phase later than $\sim$+60 d are better described by the CSM fit. However, the UV/NIR photometric coverage is too scarce to use the previous argument as discriminating factors between the two models. We notice also that the T_{min} and the v_{ejecta} values predicted by the SLSN model are in better agreement with the measured data (Figs 9 and 12) compared to those predicted in the CSM case.

Moreover, the spectra of SN 2019neq do not display the prominent narrow/multicomponent emission features seen e. g. in the luminous type-IIn SN 2006gy and SN 2006tf (Smith et al. 2007, 2008; Kiewe et al. 2012). Based on these reasons, we disfavour the CSM-interaction scenario for SN 2019neq and suggest that a millisecond magnetar endowed with a magnetic field $B \simeq 6 \times 10^{14}$ G is the engine driving the observed luminosity of SN 2019neq. CSM interaction might have contributed during pre-/post-maximum epochs and resulted in the possible complexities of the LCs of SN 2019neq. However, we cannot rule out that more peculiar (e.g. disc-like) CSM configurations might have reprocessed the UV/X-ray photons before reaching the photosphere, thus quenching the narrow/multicomponent line formation (Andrews & Smith 2018).

5 CONCLUSIONS

We analysed the spectrophotometric observations of SN 2019neq, which is among the fastest evolving SLSNe I ever observed. Its LCs rise towards maximum in about 24 rest-frame days and decline at a $\sim$2.6 times slower rate. Similar to other SLSNe I, SN 2019neq displays approximately constant blue colours during the pre-maximum/maximum epochs. At these phases, the spectra display W-shaped absorptions attributed to O II, and at a phase 16–19 d remind the spectra of SNe Ic/Ic BL at maximum luminosity. From the narrow lines attributed to the host galaxy, we inferred a metallicity $Z \sim 0.4\,Z_\odot$, a SFR $\sim 2.6\,M_\odot$ yr^{-1}, and a sSFR of ~ 2.3 Gyr^{-1} at the SN site. A late nebular spectrum of SN 2019neq was scaled in absolute specific luminosity and compared with different models computed with the SUMO single-zone, radiative-transfer code desig-

nated for nebular spectra of SNe Ic; we also used a set of analytical relations (Jerkstrand et al. 2017) to estimate the ejecta O mass. In addition, multicolour LCs of SN 2019neq were modelled with the MOSFIT tool using the CSM and SLSN modules to test the ejecta–CSM interaction and the magnetar scenarios, respectively. Based on the best-fitting results and using the inferred nebular properties as a broad prior, we conclude that the spin-down radiation of a millisecond, young magnetar with a magnetic field of $\sim 6 \times 10^{14}$ G likely powered the luminosity of SN 2019neq at around the maximum luminosity. Given the degeneracy between the ejecta mass $M_{\rm ejecta}$ and the ejecta opacity κ, it is hard to retrieve reasonable estimates, hence we provide for them the following ranges: $M_{\rm ejecta} \simeq 10 - 30\,{\rm M}_{\odot}$ and $\kappa \simeq 0.05 - 0.1\,{\rm cm}^2\,{\rm g}^{-1}$. In addition, we cannot rule out that the ejecta of SN 2019neq have interacted with a previously ejected CSM, but either this requires a peculiar CSM topology, or that its contribution is subdominant in powering the SN around maximum luminosity.

Due to their rapid photometric evolution, SLSNe I like SN 2019neq are challenging to follow up, in particular at nebular epochs. Their careful study warrants a strong observational effort which future wide-field surveys like the Legacy Survey of Space and Time at the Vera Rubin Observatory (Villar, Nicholl & Berger 2018) will allow for. In addition, a larger data set is useful to improve the statistical significance of SLSNe sample studies. These are crucial to understand the diversity of SLSNe and to unravel the physical reasons for their luminous nature.

ACKNOWLEDGEMENTS

This work is based on observations made with the Nordic Optical Telescope, owned in collaboration by the University of Turku and Aarhus University, and operated jointly by Aarhus University, the University of Turku and the University of Oslo, representing Denmark, Finland and Norway, the University of Iceland and Stockholm University at the Observatorio del Roque de los Muchachos, La Palma, Spain, of the Instituto de Astrofisica de Canarias. The data presented here were obtained in part with ALFOSC, which is provided by the Instituto de Astrofisica de Andalucia (IAA) under a joint agreement with the University of Copenhagen and NOT. Based on observations collected at Copernico and Schmidt telescopes (Asiago, Italy) of the INAF – Osservatorio Astronomico di Padova. Based on observations made with the Gran Telescopio Canarias (GTC), installed in the Spanish Observatorio del Roque de los Muchachos of the Instituto de Astrofísica de Canarias, in the island of La Palma. AF acknowledges the support by the State of Hesse within the Research Cluster ELEMENTS (Project ID 500/10.006). XW is supported by the National Natural Science Foundation of China (NSFC grants 12288102 & 12033003), Scholar Program of Beijing Academy of Science and Technology (DZ:BS202002), and Tencent Xplorer Prize. AP acknowledges support from PRIN-MIUR 2022. AMG acknowledges financial support by the European Union under the 2014–2020 ERDF Operational Programme and by the Department of Economic Transformation, Industry, Knowledge, and Universities of the Regional Government of Andalusia through the FEDER-UCA18-107404 grant. Y-ZC is supported by the National Natural Science Foundation of China (NSFC, Grant No. 12303054) and the International Centre of Supernovae, Yunnan Key Laboratory (No. 202302AN360001). MF is supported by a Royal Society-Science Foundation Ireland University Research Fellowship. EC acknowledges support of MIUR, PRIN 2017 (grant 20179ZF5KS). SM acknowledges support from the Magnus Ehrnrooth Foundation and the Vilho, Yrjö, and Kalle Väisälä Foundation. TMR acknowledges the financial support of the Vilho, Yrjö and Kalle Väisälä Foundation of the Finnish academy of Science and Letters through the Finnish postdoc pool. IS is supported by fundings from MIUR, PRIN 2017 (grant 20179ZF5KS), by the PRIN-INAF 2022 project 'Shedding light on the nature of gap transients: from the observations to the models', and by the doctoral grant funded by Istituto Nazionale di Astrofisica via the University of Padova and the Italian Ministry of Education, University and Research (MIUR). NER acknowledges partial support from MIUR, PRIN 2017 (grant 20179ZF5KS) 'The new frontier of the Multi-Messenger Astrophysics: follow-up of electromagnetic transient counterparts of gravitational wave sources.', from PRIN-INAF 2022 'Shedding light on the nature of gap transients: from the observations to the models', from the Spanish MICINN grant PID2019-108709GB-I00 and FEDER funds, and from the program Unidad de Excelencia María de Maeztu CEX2020-001058-M. CPG acknowledges financial support from the Secretary of Universities and Research (Government of Catalonia) and by the Horizon 2020 Research and Innovation Programme of the European Union under the Marie Skłodowska-Curie and the Beatriu de Pinós 2021 BP 00168 programme, from the Spanish Ministerio de Ciencia e Innovación (MCIN) and the Agencia Estatal de Investigación (AEI) 10.13039/501100011033 under the PID2020-115253GA-I00 HOSTFLOWS project, and the program Unidad de Excelencia María de Maeztu CEX2020-001058.

DATA AVAILABILITY

The data presented in this paper and listed in Appendices A, B are available in the online supplementary material. The spectra will be made public via WISEREP (Yaron & Gal-Yam 2012).

REFERENCES

Andrews J. E., Smith N., 2018, MNRAS, 477, 74
Angus C. R. et al., 2019, MNRAS, 487, 2215
Asplund M., Grevesse N., Sauval A. J., Scott P., 2009, ARA&A, 47, 481
Becker A., 2015, Astrophysics Source Code Library, record ascl:1504.004
Bellm E. C. et al., 2019, PASP, 131, 018002
Bianco F. B., Modjaz M., Oh S. M., Fierroz D., Liu Y. Q., Kewley L., Graur O., 2016, Astron. Comput., 16, 54
Calzetti D., Kinney A. L., Storchi-Bergmann T., 1994, ApJ, 429, 582
Cappellaro E., 2014, snoopy: a package for SN photometry. Available at: http://sngroup.oapd.inaf.it/snoopy.html
Cepa J. et al., 2000, in Iye M., Moorwood A. F., eds, Proc. SPIE Conf. Ser. Vol. 4008, Optical and IR Telescope Instrumentation and Detectors. SPIE, Bellingham, p. 623
Chambers K. C. et al., 2016, preprint (arXiv:1612.05560)
Chatzopoulos E., Wheeler J. C., Vinko J., 2012, ApJ, 746, 121
Chatzopoulos E., Wheeler J. C., Vinko J., Horvath Z. L., Nagy A., 2013, ApJ, 773, 76
Chen T. W. et al., 2015, MNRAS, 452, 1567
Chen T.-W., Smartt S. J., Yates R. M., Nicholl M., Krühler T., Schady P., Dennefeld M., Inserra C., 2017, MNRAS, 470, 3566
Chen Z. H. et al., 2023a, ApJ, 943, 41
Chen Z. H. et al., 2023b, ApJ, 943, 42
Chomiuk L. et al., 2011, ApJ, 743, 114
Chonis T. S., Gaskell C. M., 2008, AJ, 135, 264
De Cia A. et al., 2018, ApJ, 860, 100
Dessart L., Hillier D. J., Waldman R., Livne E., Blondin S., 2012, MNRAS, 426, L76
Dessart L., Hillier D. J., Woosley S., Livne E., Waldman R., Yoon S.-C., Langer N., 2015, MNRAS, 453, 2189
Elias-Rosa N. et al., 2006, MNRAS, 369, 1880
Fiore A. et al., 2021, MNRAS, 502, 2120
Fiore A. et al., 2022, MNRAS, 512, 4484
Gal-Yam A., 2012, Science, 337, 927
Gal-Yam A., 2019, ARA&A, 57, 305

Gal-Yam A. et al., 2009, Nature, 462, 624
Gehrels N. et al., 2004, ApJ, 611, 1005
Guillochon J., Nicholl M., Villar V. A., Mockler B., Narayan G., Mandel K. S., Berger E., Williams P. K. G., 2017a, Astrophysics Source Code Library, record ascl:1710.006
Guillochon J., Parrent J., Kelley L. Z., Margutti R., 2017b, ApJ, 835, 64
Gutiérrez C. P. et al., 2022, MNRAS, 517, 2056
Harutyunyan A. H. et al., 2008, A&A, 488, 383
Hogg D. W., Baldry I. K., Blanton M. R., Eisenstein D. J., 2002, preprint (arXiv:astro-ph/0210394)
Holmbo S. et al., 2019, Astron. Telegram, 12661, 1
Hosseinzadeh G., Berger E., Metzger B. D., Gomez S., Nicholl M., Blanchard P., 2022, ApJ, 933, 14
Huang F. et al., 2015, ApJ, 807, 59
Inserra C. et al., 2013, ApJ, 770, 128
Inserra C., Prajs S., Gutierrez C. P., Angus C., Smith M., Sullivan M., 2018, ApJ, 854, 175
Jerkstrand A. et al., 2017, ApJ, 835, 13
Kasen D., Bildsten L., 2010, ApJ, 717, 245
Kasen D., Woosley S. E., Heger A., 2011, ApJ, 734, 102
Kennicutt R. C., Jr, 1998, ARAA, 36, 189
Kessler R. et al., 2015, AJ, 150, 172
Khetan N. et al., 2021, A&A, 647, A72
Kiewe M. et al., 2012, ApJ, 744, 10
Könyves-Tóth R., 2022, ApJ, 940, 69
Könyves-Tóth R., Vinkó J., 2021, ApJ, 909, 24
Könyves-Tóth R., Vinko J., Thomas B. P., Wheeler J. C., 2019, Astron. Telegram, 13085, 1
Könyves-Tóth R., Thomas B. P., Vinkó J., Wheeler J. C., 2020, ApJ, 900, 73
Kozyreva A., Blinnikov S., 2015, MNRAS, 454, 4357
Kumar A. et al., 2020, ApJ, 892, 28
Leloudas G. et al., 2012, A&A, 541, A129
Lin W. L. et al., 2020, MNRAS, 497, 318
Lin W. et al., 2023, Nat. Astron., 7, 779
Liu L.-D., Zhang B., Wang L.-J., Dai Z.-G., 2018, ApJ, 868, L24
Lunnan R. et al., 2014, ApJ, 787, 138
Lunnan R. et al., 2018, ApJ, 852, 81
Lunnan R. et al., 2020, ApJ, 901, 61
Maiolino R. et al., 2008, A&A, 488, 463
Mattila S. et al., 2016, Astron. Telegram, 8992, 1
Mazzali P. A., Sullivan M., Pian E., Greiner J., Kann D. A., 2016, MNRAS, 458, 3455
Mazzali P. A., Moriya T. J., Tanaka M., Woosley S. E., 2019, MNRAS, 484, 3451
Moriya T. J., Mazzali P. A., Tanaka M., 2019, MNRAS, 484, 3443
Moriya T. J., Murase K., Kashiyama K., Blinnikov S. I., 2022, MNRAS, 513, 6210
Nadyozhin D. K., 1994, ApJS, 92, 527
Nagy A. P., 2018, ApJ, 862, 143
NASA High Energy Astrophysics Science Archive Research Center (HEASARC), 2014, Astrophysics Source Code Library, record ascl:1408.004
Nicholl M. et al., 2013, Nature, 502, 346
Nicholl M. et al., 2014, MNRAS, 444, 2096
Nicholl M. et al., 2015a, MNRAS, 452, 3869
Nicholl M. et al., 2015b, ApJ, 807, L18
Nicholl M. et al., 2016a, ApJ, 826, 39
Nicholl M. et al., 2016b, ApJ, 828, L18
Nicholl M., Guillochon J., Berger E., 2017, ApJ, 850, 55
Pastorello A. et al., 2010, ApJ, 724, L16
Perley D. A. et al., 2019, Transient Name Server AstroNote, 79, 1
Piascik A. S., Steele I. A., Bates S. D., Mottram C. J., Smith R. J., Barnsley R. M., Bolton B., 2014, in Ramsay S. K., McLean I. S., Takami H., eds, Proc. SPIE Conf. Ser. Vol. 9147, Ground-based and Airborne Instrumentation for Astronomy V. SPIE, Bellingham, p. 91478H
Pignata G. et al., 2004, MNRAS, 355, 178
Planck Collaboration XIII, 2016, A&A, 594, A13
Poznanski D., Prochaska J. X., Bloom J. S., 2012, MNRAS, 426, 1465
Pursiainen M. et al., 2023, A&A, 674, A81
Quimby R. M. et al., 2011, Nature, 474, 487
Quimby R. M. et al., 2018, ApJ, 855, 2
Riess A. G., Casertano S., Yuan W., Bowers J. B., Macri L., Zinn J. C., Scolnic D., 2021, ApJ, 908, L6
Sahu D. K., Tanaka M., Anupama G. C., Gurugubelli U. K., Nomoto K., 2009, ApJ, 697, 676
Savitzky A., Golay M. J. E., 1964, Anal. Chem., 36, 1627
Schlafly F. E., Finkbeiner D. P., 2011, ApJ, 737, 103
Skrutskie M. F. et al., 2006, AJ, 131, 1163
Smith M. et al., 2016, ApJ, 818, L8
Smith N. et al., 2007, ApJ, 666, 1116
Smith N., Chornock R., Li W., Ganeshalingam M., Silverman J. M., Foley R. J., Filippenko A. V., Barth A. J., 2008, ApJ, 686, 467
Sorokina E., Blinnikov S., Nomoto K., Quimby R., Tolstov A., 2016, ApJ, 829, 17
Steele I. A. et al., 2004, in Oschmann J. M., Jr, ed., Proc. SPIE Conf. Ser. Vol. 5489, Ground-based Telescopes. SPIE, Bellingham, p. 679
Stetson P. B., 1987, PASP, 99, 191
Stritzinger M. et al., 2002, AJ, 124, 2100
Szentgyorgyi A. H. et al., 2005, American Astronomical Society Meeting Abstracts, #110.10
Taylor E. N. et al., 2011, MNRAS, 418, 1587
Tolstov A., Nomoto K., Blinnikov S., Sorokina E., Quimby R., Baklanov P., 2017, ApJ, 835, 266
Tonry J. L. et al., 2018a, PASP, 130, 064505
Tonry J. L. et al., 2018b, ApJ, 867, 105
Umeda H., Nomoto K., 2008, ApJ, 673, 1014
Valenti S. et al., 2008, MNRAS, 383, 1485
Villar V. A., Nicholl M., Berger E., 2018, ApJ, 869, 166
Vreeswijk P. M. et al., 2017, ApJ, 835, 58
Wang X. et al., 2008, ApJ, 675, 626
West S. L. et al., 2023, A&A, 670, A7
Woosley S. E., 2017, ApJ, 836, 244
Woosley S. E., Blinnikov S., Heger A., 2007, Nature, 450, 390
Yan L. et al., 2015, ApJ, 814, 108
Yan L. et al., 2017, ApJ, 848, 6
Yaron O., Gal-Yam A., 2012, PASP, 124, 668
Yoshida T., Umeda H., Maeda K., Ishii T., 2016, MNRAS, 457, 351

SUPPORTING INFORMATION

Supplementary data are available at *MNRAS* online.

Table C1. *uvw*1, *uvm*2, *uvw*2-filters observed (non K-corrected, non S-corrected) aperture magnitudes (in AB system).
Table C2. *u*, *g*, *r*, *i*, *z*-filter observed (non K-corrected, non S-corrected) magnitudes (in AB system). Errors are in parentheses.
Table C3. *U*, *B*, *V*-observed (non K-corrected, non S-corrected) magnitudes (in AB system).
Table C4. NIR-observed (non K-corrected) *J*, *H*, *K* magnitudes (in AB system).
Table C5. S-corrections for Schmidt and AFOSC filters.
Table C6. S-corrections for ALFOSC.
Table C7. S-corrections for IO:O filters.
Table C8. S-corrections for *Swift*/UVOT filters.
Table C9. Estimated uncertainties $\Delta S_{\rm corr}$ for the filters *u*, *U*, *z*, *J*, *H*, $K_{\rm s}$ (for each instrument) divided in two temperature ranges.
Table C10. corrections expressed in magnitudes.
Table C11. Logarithm of the bolometric luminosity of SN 2019neq integrated over the *uvw*2, *uvm*2, *uvw*1, *U*, *B*, *g*, *V*, *r*, *i*, *z*, *J*, *H*, $K_{\rm s}$ filters.

Please note: Oxford University Press is not responsible for the content or functionality of any supporting materials supplied by the authors.

Any queries (other than missing material) should be directed to the corresponding author for the article.

APPENDIX A: S-CORRECTIONS AND K-CORRECTIONS

A1 S-correction

As different instrumental setups correspond to different photometric systems, we computed the S-correction (see e.g. Stritzinger et al. 2002; Pignata et al. 2004; Elias-Rosa et al. 2006) to bring back all the magnitude measurements to a standard system. In this work, we define the S-correction as $S_{\rm corr} = m_{s,\rm standard} - m_{s,\rm instr}$, where $m_{s,\rm standard}$ and $m_{s,\rm instr}$ are synthetic photometry measurements performed on the spectra using the instrumental and the standard filter, respectively (see Fig. A1). The S-correction values are secured in Tables C5,C6, C7, C8. These were linearly interpolated for the photometric epochs not matched by coeval spectroscopic ones. The $S_{\rm corr}$ values were then summed to the measured magnitudes and its statistical dispersion ($\lesssim$ 0.01 magnitudes) was propagated in our analysis (see Table C9).

Finally, for the filters where the wavelength range falls at least partly outside the spectral coverage, we computed the S-correction as before, but using a blackbody as the spectrum on which synthetic photometry was performed. The maximum value for the S-correction computed using a blackbody $\Delta S_{\rm corr}$ was evaluated in two temperature ranges ($5000\,{\rm K} < T < 8000\,{\rm K}$ and $8000\,{\rm K} < T < 12\,000\,{\rm K}$, see also Section 4.2) and propagated in our analysis as an additional uncertainty due to the non-standard instrumental photometric systems.

A2 K-correction

We computed K-corrections to account for the effect of the cosmological redshift on the magnitude measured in the observer frame bandpass filters. Similar to S-corrections, we computed the K-corrections performing synthetic magnitudes measurements on the spectra of SN 2019neq (see Section 3) via PYSYNPHOT. In detail, for each bandpass filter, we derived a synthetic magnitude both for the rest-frame spectrum (for which we computed a synthetic magnitude $m_{s,\rm rest}$) and for the observed one (for which we computed a synthetic magnitude $m_{s,\rm obs}$). For each epoch and filter, the K-correction was computed as $m_{s,\rm rest} - m_{s,\rm obs}$. The resulting K-corrections are listed in Table C10. Similar to the $\Delta S_{\rm corr}$, the K-corrections for the *uvw*2, *uvm*2, *uvw*1, *J*, *H*, $K_{\rm s}$-filter magnitudes were estimated as before but using blackbody fits to the SED.

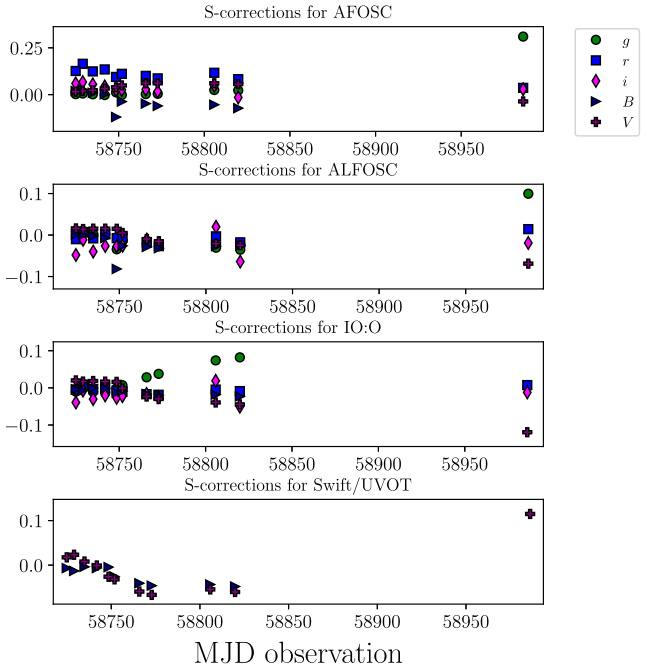

Figure A1. S-corrections for SN 2019neq for the different instrumental configurations used for the photometric follow-up of SN 2019neq.

APPENDIX B: FIGURES

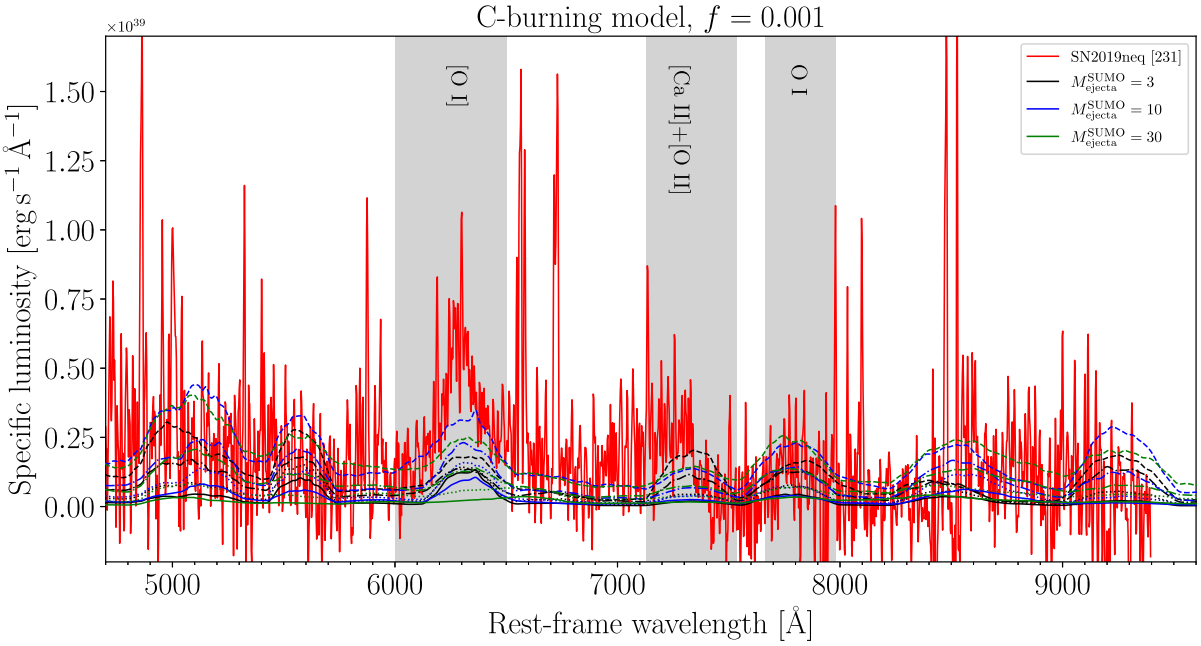

Figure B1. Comparison of the observed nebular spectrum of SN 2019neq (red line) with different SUMO spectra computed for the C-burning model with a filling factor $f = 0.001$ for different ejecta masses $M_{\rm ejecta}^{\rm SUMO} = 10, 30$ and different energy depositions $E_{\rm dep}$. Different colours correspond to different $M_{\rm ejecta}^{\rm SUMO}$, as labelled in the top-right corner. Solid lines correspond to an energy deposition $E_{\rm dep} = 2.5 \times 10^{41}$ erg s^{-1}, dotted lines to $E_{\rm dep} = 5 \times 10^{41}$ erg s^{-1}, dashed-dotted lines to $E_{\rm dep} = 1 \times 10^{42}$ erg s^{-1}, dashed lines to $E_{\rm dep} = 2 \times 10^{42}$ erg s^{-1}. A color version of the figure is available in the online version.

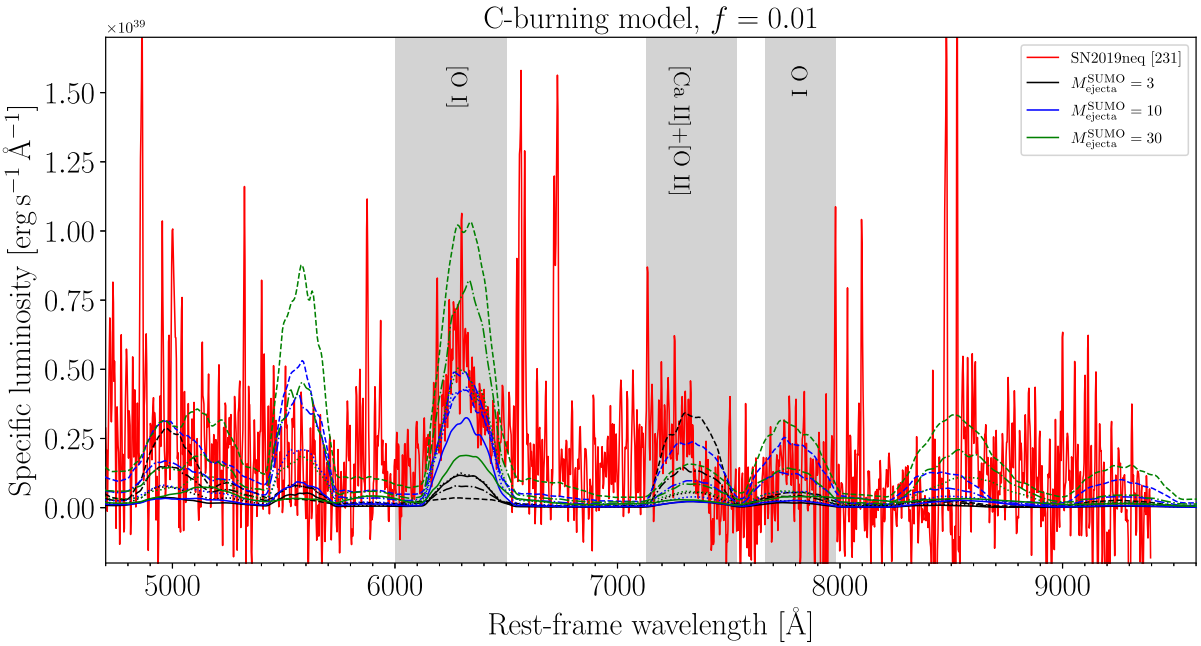

Figure B2. Similar to Fig. B1, but for the C-burning model and $f = 0.01$.

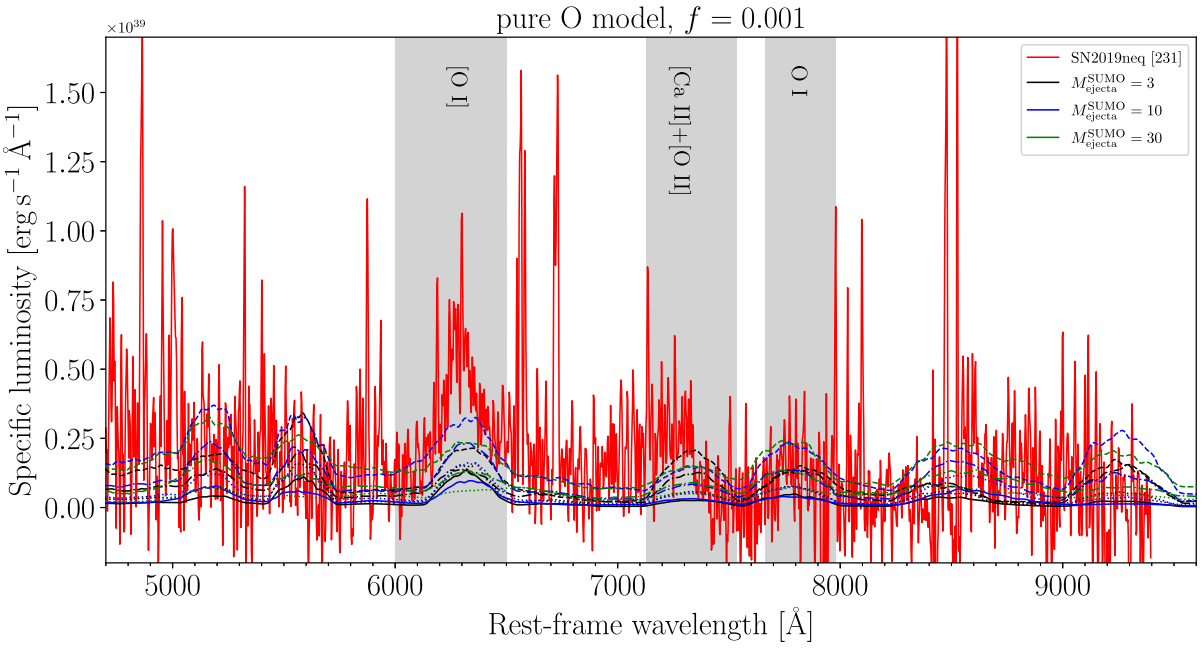

Figure B3. Similar to Fig. B1, but for the pure-Oxygen model.

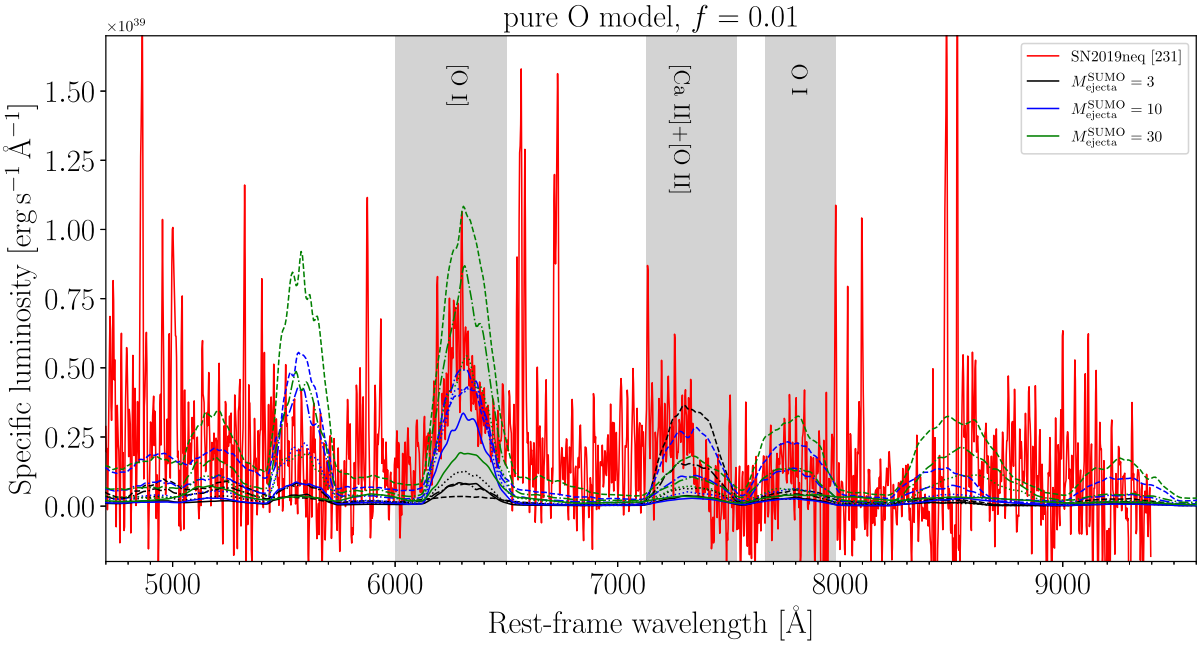

Figure B4. Similar to Fig. B1, but for the pure-Oxygen model and $f = 0.01$.

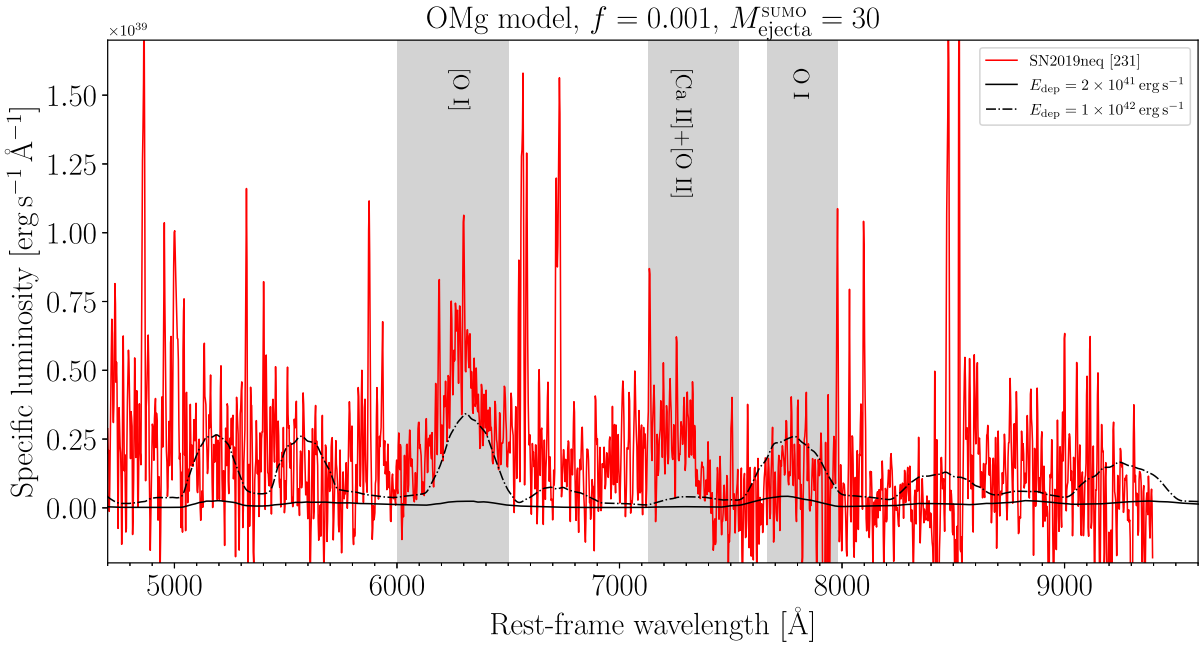

Figure B5. Similar to Fig. B1, but for the OMg model and $M_{\rm ejecta}^{\rm SUMO} = 30$. Here the solid line corresponds to an energy deposition $E_{\rm dep} = 2 \times 10^{41}$ erg s^{-1}.

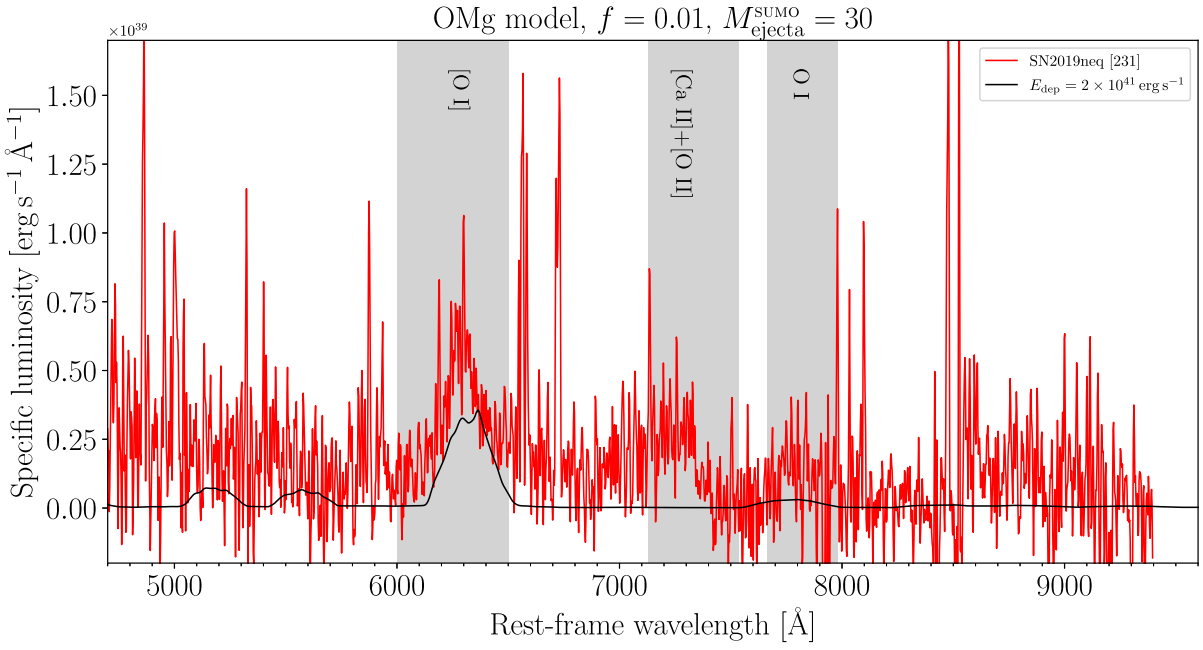

Figure B6. Similar to Fig. B1, but for the OMg model, $f = 0.01$ and $M_{\rm ejecta}^{\rm SUMO} = 30$. Here the solid line corresponds to an energy deposition $E_{\rm dep} = 2 \times 10^{41}$ erg s^{-1}.

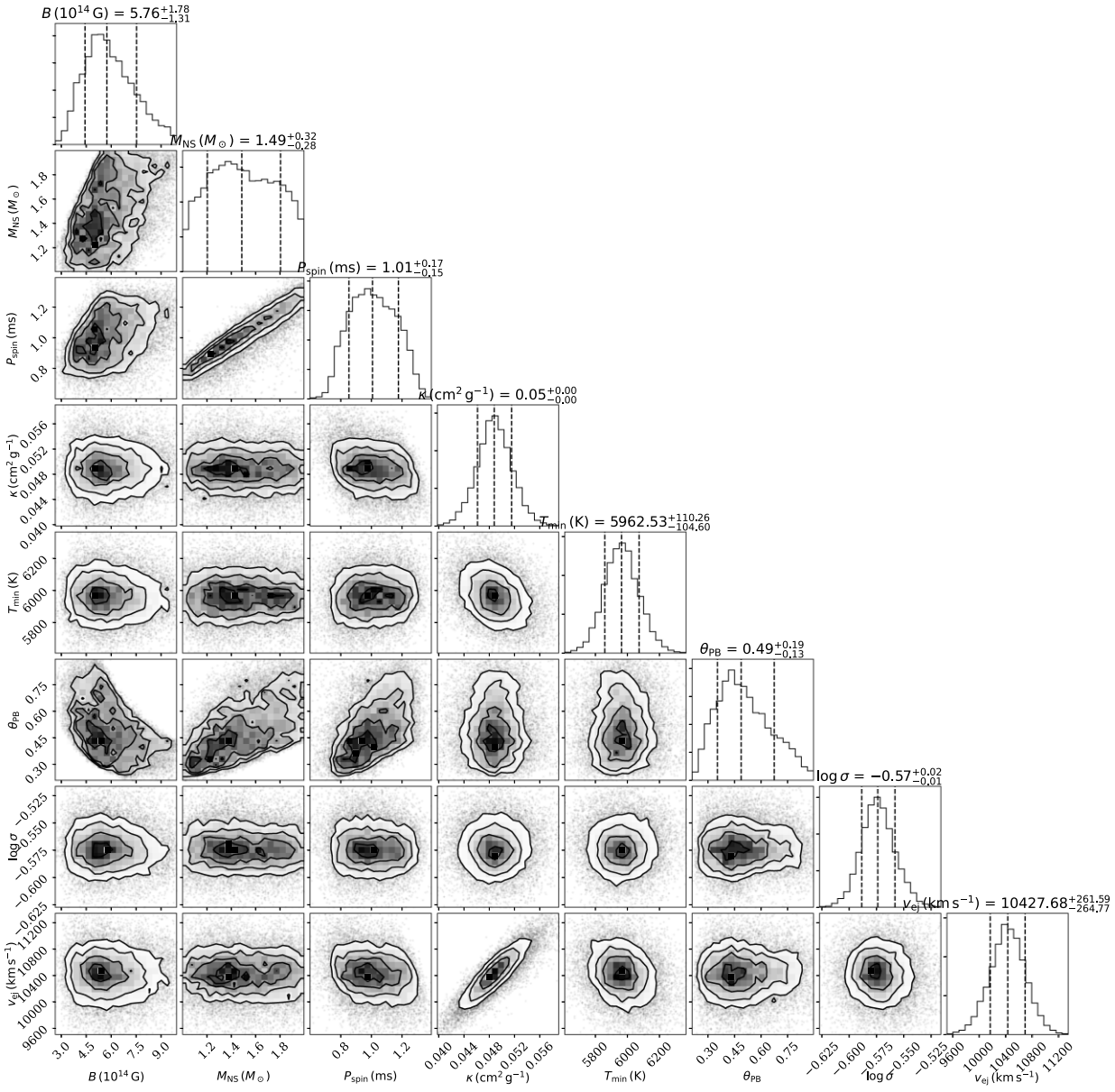

Figure B7. Corner plot with the best-fitting parameters of the MOSFIT fit obtained with the SLSN model.

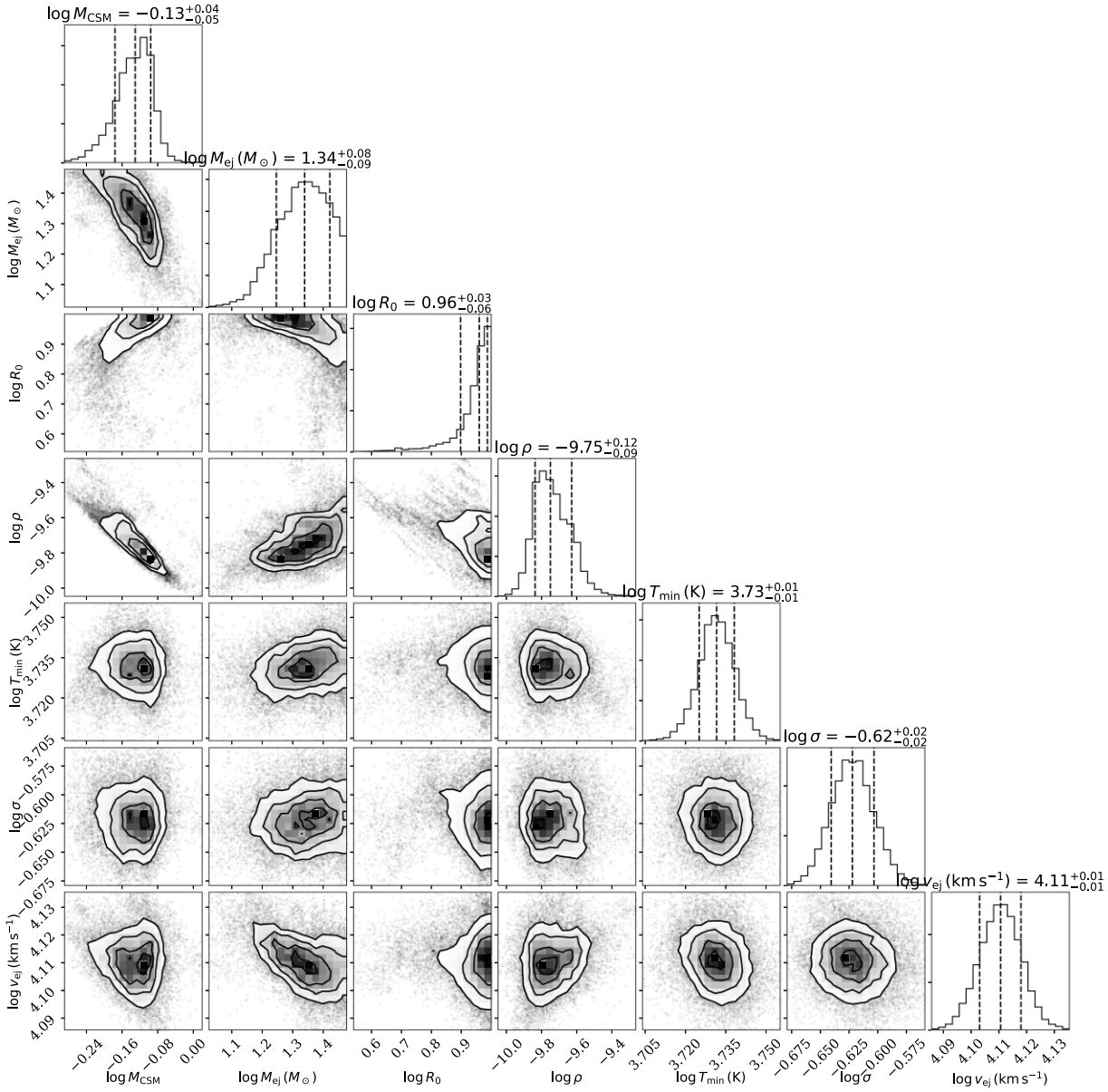

Figure B8. Same as Fig. B7, but for the CSM fit.

APPENDIX C: TABLES

Table C1. *uvw*1, *uvm*2, *uvw*2-filters observed (non K-corrected, non S-corrected) aperture magnitudes (in AB system). Errors are in parentheses. The full table is available online as supplementary material.

MJD	Phase (d)	*uvw*1	*uvm*2	*uvw*2	Instrument
58729.66	− 1.21	17.65 (0.07)	18.26 (0.07)	18.85 (0.09)	*Swift*/UVOT
58732.68	1.52	17.88 (0.07)	18.44 (0.07)	18.82 (0.09)	*Swift*/UVOT
58734.36	3.04	18.03 (0.08)	18.52 (0.08)	18.95 (0.10)	*Swift*/UVOT
...	...	...	...	...	...

Table C2. *u*, *g*, *r*, *i*, *z*-filter observed (non K-corrected, non S-corrected) magnitudes (in AB system). Errors are in parentheses. The full table is available online as supplementary material.

MJD	Phase (d)	*u*	*g*	*r*	*i*	*z*	Instrument
58617.43	−102.69	–	$\gtrsim$ 22.39	–	–	–	ZTF
58644.22	−78.47	–	$\gtrsim$ 22.36	–	–	–	ZTF
58651.21	−72.15	–	$\gtrsim$ 20.45	–	–	–	ZTF
...	...	...	...	...	...	...	...

Table C3. *U*, *B*, *V*-observed (non K-corrected, non S-corrected) magnitudes (in AB system). *Swift*/UVOT photometry was measured with a 5 arcsec radius aperture (see the text). Errors are in parentheses. The full table is available online as supplementary material.

MJD	Phase (d)	*U*	*B*	*V*	Instrument
58728.51	−2.25	–	17.27 (0.01)	17.15 (0.01)	TNT
58729.07	−1.75	–	17.14 (0.03)	17.16 (0.02)	AFOSC
58729.54	−1.32	–	17.17 (0.01)	17.10 (0.02)	TNT
...	...	...	...	...	...

Table C4. NIR-observed (non K-corrected) *J*, *H*, *K* magnitudes (in AB system). Errors are in parentheses. The full table is available online as supplementary material.

MJD	Phase (d)	*J*	*H*	K_s	Instrument
58760.82	26.96	16.95 (0.03)	–	18.86 (0.06)	NOT + NOTCAM
58780.45	44.71	18.32 (0.04)	18.81 (0.04)	19.29 (0.07)	NOT + NOTCAM
58803.81	65.84	18.81 (0.07)	19.17 (0.08)	19.19 (0.09)	NOT + NOTCAM
...	...	...	...	...	...

Table C5. S-corrections for Schmidt and AFOSC filters. The full table is available online as supplementary material.

MJD	*B*	*g*	*V*	*r*	*i*
58729.05	0.03	0.01	0.02	0.16	0.07
58748.49	−0.12	0.01	0.04	0.09	0.02
58724.91	0.02	0.00	0.02	0.13	0.06
...	...	...	...	...	...

Table C6. S-corrections for ALFOSC. The full table is available online as supplementary material.

MJD	*B*	*g*	*V*	*r*	*i*
58729.05	0.00	0.01	0.01	0.01	−0.01
58748.49	−0.08	−0.03	0.02	−0.01	−0.03
58724.91	0.00	0.01	0.02	−0.01	−0.05
...	...	...	...	...	...

Table C7. S-corrections for IO:O filters. The full table is available online as supplementary material.

MJD	*B*	*g*	*V*	*r*	*i*
58729.05	−0.01	0.00	0.02	0.00	−0.01
58748.49	−0.01	0.00	0.02	−0.01	−0.03
58724.91	−0.00	0.01	0.02	−0.00	−0.04
...	...	...	...	...	...

Table C8. S-corrections for *Swift*/UVOT filters. The full table is available online as supplementary material.

MJD	*B*	*V*
58729.05	−0.01	0.02
58748.49	−0.00	−0.03
58724.91	−0.01	0.02
...	...	...

Table C9. Estimated uncertainties $\Delta S_{\rm corr}$ for the filters *u*, *U*, *z*, *J*, *H*, K_s (for each instrument) divided in two temperature ranges. The full table is available online as supplementary material.

	5000 K < *T* < 8000 K	8000 K < *T* < 12000 K
NOT + ALFOSC/NOTCam	$\Delta S_{{\rm corr},u} = 0.05$	$\Delta S_{{\rm corr},u} = 0.15$
	$\Delta S_{{\rm corr},z} = 0.01$	$\Delta S_{{\rm corr},z} = 0.02$
	$\Delta S_{{\rm corr},J} = 0.1$	$\Delta S_{{\rm corr},J} = 0.1$
	$\Delta S_{{\rm corr},H} = 0.1$	$\Delta S_{{\rm corr},H} = 0.1$
	$\Delta S_{{\rm corr},K_s} = 0.1$	$\Delta S_{{\rm corr},K_s} = 0.1$
...	...	...

Table C10. K-corrections expressed in magnitudes. The full table is available online as supplementary material.

Phase maximum (d)	*uvw*2 filter	*uvm*2 filter	*uvw*1 filter	*u* filter	*U* filter	*B* filter	*g* filter	*V* filter	*r* filter	*i* filter	*z* filter	*J* filter	*H* filter	K_s filter
−6.07	−0.12	−0.21	−0.22	0.01	−0.15	−0.15	−0.10	−0.15	−0.10	−0.19	0.22	0.25	0.28	0.29
−1.95	−0.16	−0.26	−0.26	−0.03	−0.15	−0.15	−0.10	−0.15	−0.10	−0.19	0.21	0.25	0.27	0.29
3.92	−0.16	−0.26	−0.26	−0.03	−0.11	−0.11	−0.09	−0.11	−0.09	−0.17	0.21	0.25	0.27	0.29
...	...	...	...	...	...	...	...	...	...	...	...	...	...	...

Table C11. Logarithm of the bolometric luminosity of SN 2019neq integrated over the *uvw*2, *uvm*2, *uvw*1, *U*, *B*, *g*, *V*, *r*, *i*, *z*, *J*, *H*, K_s filters. The full table is available online as supplementary material.

Phase (d)	$\log_{10}L_{bol}$
−22.80	43.35 (0.02)
−22.80	43.35 (0.02)
−21.80	43.45 (0.02)
...	...

Table C12. Spectra in Fig. 3.

MJD	Phase (d)	Instrument	Resolution (Å)
58724.0	−6	ALFOSC [gr4]	15
58729.0	−2	AFOSC [VPH6 + VPH7]	18
58734.9	4	ALFOSC [gr4]	19
58741.9	10	ALFOSC [gr4]	15
58748.5	16	BFOSC [G4]	–
58751.9	19	ALFOSC [gr4]	18
58765.9	32	ALFOSC [gr4]	15
58772.8	38	ALFOSC [gr4]	15
58805.8	68	ALFOSC [gr4]	25
58819.8	80	OSIRIS [R1000I]	8
58986.1	231	OSIRIS [R1000R]	9

[1]*Institut für Theoretische Physik, Goethe Universität, Max-von-Laue-Str. 1, D-60438 Frankfurt am Main, Germany*
[2]*INAF – Osservatorio Astronomico di Padova, Vicolo dell'Osservatorio 5, I-35122 Padova, Italy*
[3]*INAF – Osservatorio Astronomico d'Abruzzo, via M. Maggini snc, I-64100 Teramo, Italy*
[4]*The Oskar Klein Centre, Department of Astronomy, Stockholm University, AlbaNova, SE-10691 Stockholm, Sweden*
[5]*Dipartimento di Fisica e Astronomia 'G. Galilei', Università di Padova, Vicolo dell'Osservatorio 3, I-35122 Padova, Italy*
[6]*Department of Applied Physics, School of Engineering, University of Cádiz, Campus of Puerto Real, E-11519 Cádiz, Spain*
[7]*Instituto de Astrofisíca de Canarias, E-38200 La Laguna, Tenerife, Canary Islands, Spain*
[8]*GRANTECAN: Cuesta de San José s/n, E-38712 Breña Baja, La Palma, Spain*
[9]*Institute of Space Sciences (ICE, CSIC), Campus UAB, Carrer de Can Magrans s/n, E-08193 Barcelona, Spain*
[10]*Physics Department and Tsinghua Center for Astrophysics (THCA), Tsinghua University, Beijing 100084, China*
[11]*Beijing Planetarium, Beijing Academy of Science and Technology, Beijing 100044, China*
[12]*Astrophysics Research Institute, Liverpool John Moores University, Liverpool L3 5RF, UK*
[13]*Max-Planck-Institut für Astrophysik, Karl-Schwarzschild Str.1, D-85748, Garching, Germany*
[14]*INFN – Sezione di Padova, Via Francesco Marzolo 8, I-35131 Padova, Italy*
[15]*Yunnan Observatories, Chinese Academy of Sciences, Kunming 650216, P. R. China*
[16]*Key Laboratory for the Structure and Evolution of Celestial Objects, Chinese Academy of Sciences, Kunming 650216, P. R. China*
[17]*International Centre of Supernovae, Yunnan Key Laboratory, Kunming 650216, P. R. China*
[18]*UCD School of Physics, L.M.I. Main Building, Beech Hill Road, Dublin 4, D04 P7W1, Ireland*
[19]*Institut d'Estudis Espacials de Catalunya (IEEC), Gran Capità, 2-4, Edifici Nexus, Desp. 201, E-08034 Barcelona, Spain*
[20]*Institute of Space Sciences (ICE, CSIC), Campus UAB, Carrer de Can Magrans, s/n, E-08193 Barcelona, Spain*
[21]*Department of Physics and Astronomy, Aarhus University, Ny Munkegade 120, DK-8000 Aarhus C, Denmark*
[22]*Department of Physics and Astronomy, University of Turku, Vesilinnantie 5, FI-20500 Turku, Finland*
[23]*INAF – Osservatorio Astronomico di Brera, Via Bianchi 46, I-23807 Merate (LC), Italy*
[24]*Cosmic DAWN Centre, Niels Bohr Institute, University of Copenhagen, Rådmandsgade, 62-64, DK-2200 Copenhagen, Denmark*

This paper has been typeset from a TEX/LATEX file prepared by the author.